2013-12

Dynamics, heat transport, spectral composition and acoustic signatures of mesoscale variability in the ocean

Carvalho, Daniel Peixoto de

Monterey, California. Naval Postgraduate School

NAVAL POSTGRADUATE SCHOOL

MONTEREY, CALIFORNIA

THESIS

DYNAMICS, HEAT TRANSPORT, SPECTRAL COMPOSITION AND ACOUSTIC SIGNATURES OF MESOSCALE VARIABILITY IN THE OCEAN

by

Daniel Peixoto de Carvalho

December 2013

Thesis Advisor: Timour Radko
Second Reader: John Joseph

Approved for public release; distribution is unlimited

THIS PAGE INTENTIONALLY LEFT BLANK

REPORT DOCUMENTATION PAGE			Form Approved OMB No. 0704-0188
Public reporting burden for this collection of information is estimated to average 1 hour per response, including the time for reviewing instruction, searching existing data sources, gathering and maintaining the data needed, and completing and reviewing the collection of information. Send comments regarding this burden estimate or any other aspect of this collection of information, including suggestions for reducing this burden, to Washington headquarters Services, Directorate for Information Operations and Reports, 1215 Jefferson Davis Highway, Suite 1204, Arlington, VA 22202-4302, and to the Office of Management and Budget, Paperwork Reduction Project (0704-0188) Washington DC 20503.			
1. AGENCY USE ONLY *(Leave blank)*	**2. REPORT DATE** December 2013	**3. REPORT TYPE AND DATES COVERED** Master's Thesis	
4. TITLE AND SUBTITLE DYNAMICS, HEAT TRANSPORT, SPECTRAL COMPOSITION AND ACOUSTIC SIGNATURES OF MESOSCALE VARIABILITY IN THE OCEAN		**5. FUNDING NUMBERS**	
6. AUTHOR(S) Daniel Peixoto de Carvalho			
7. PERFORMING ORGANIZATION NAME(S) AND ADDRESS(ES) Naval Postgraduate School Monterey, CA 93943-5000		**8. PERFORMING ORGANIZATION REPORT NUMBER**	
9. SPONSORING /MONITORING AGENCY NAME(S) AND ADDRESS(ES) N/A		**10. SPONSORING/MONITORING AGENCY REPORT NUMBER**	
11. SUPPLEMENTARY NOTES The views expressed in this thesis are those of the author and do not reflect the official policy or position of the Department of Defense or the U.S. Government. IRB Protocol number ____N/A____.			
12a. DISTRIBUTION / AVAILABILITY STATEMENT Approved for public release; distribution is unlimited		**12b. DISTRIBUTION CODE**	

13. ABSTRACT (maximum 200 words)

The general circulation of the global ocean is turbulent rather than laminar. Mesoscale eddies contribute to the transport of tracers like heat, salt, and oxygen, and affect large-scale ocean dynamics. The problem of representing mesoscale variability stems from the nonlinear character of eddy dynamics that makes it difficult to predict equilibrated fluxes. The most intuitive solution is to apply a parameterization based on the eddy-driven transport observed in a global ocean that has been spinning up for centuries, which may not be feasible at present. An alternative approach involves constructing relatively simple analytically tractable equilibration models. In this study, the equilibration mechanism called the Growth Rate Balance (GRB) model proposes an explanation to the eddy dynamics as a competition between primary and secondary instabilities. The GRB model is validated in two configurations: in a two-layer model, and in a continuously stratified model. They identify the dependences of equilibrated fluxes on the characteristics of the background flow, and the applicability range of the GRB model. Finally, acoustic signatures of a fully developed eddy field predicted by the GRB model characterize the role of mesoscale variability in the important naval problem of acoustic propagation.

14. SUBJECT TERMS Mesoscale Variability, Mesoscale Eddies, Eddy-Induced Fluxes, Eddy-Induced Transports, Eddy Development, Equilibration Mechanism, Instability Growth, Growth Rate Balance, GRB model			**15. NUMBER OF PAGES** 79
			16. PRICE CODE
17. SECURITY CLASSIFICATION OF REPORT Unclassified	**18. SECURITY CLASSIFICATION OF THIS PAGE** Unclassified	**19. SECURITY CLASSIFICATION OF ABSTRACT** Unclassified	**20. LIMITATION OF ABSTRACT** UU

NSN 7540-01-280-5500 Standard Form 298 (Rev. 2-89)
Prescribed by ANSI Std. 239-18

THIS PAGE INTENTIONALLY LEFT BLANK

Approved for public release; distribution is unlimited

DYNAMICS, HEAT TRANSPORT, SPECTRAL COMPOSITION AND ACOUSTIC SIGNATURES OF MESOSCALE VARIABILITY IN THE OCEAN

Daniel Peixoto de Carvalho
Lieutenant Commander, Brazilian Navy
B.S., Brazilian Naval Academy, 2000

Submitted in partial fulfillment of the
requirements for the degree of

MASTER OF SCIENCE IN METEOROLOGY AND PHYSICAL OCEANOGRAPHY

from the

NAVAL POSTGRADUATE SCHOOL
December 2013

Author: Daniel Peixoto de Carvalho

Approved by: Timour Radko
Thesis Advisor

John Joseph
Second Reader

Peter Chu
Chair, Department of Oceanography

THIS PAGE INTENTIONALLY LEFT BLANK

ABSTRACT

The general circulation of the global ocean is turbulent rather than laminar. Mesoscale eddies contribute to the transport of tracers like heat, salt, and oxygen, and affect large-scale ocean dynamics. The problem of representing mesoscale variability stems from the nonlinear character of eddy dynamics that makes it difficult to predict equilibrated fluxes. The most intuitive solution is to apply a parameterization based on the eddy-driven transport observed in a global ocean that has been spinning up for centuries, which may not be feasible at present. An alternative approach involves constructing relatively simple analytically tractable equilibration models. In this study, the equilibration mechanism called the Growth Rate Balance (GRB) model proposes an explanation to the eddy dynamics as a competition between primary and secondary instabilities. The GRB model is validated in two configurations: in a two-layer model, and in a continuously stratified model. They identify the dependences of equilibrated fluxes on the characteristics of the background flow, and the applicability range of the GRB model. Finally, acoustic signatures of a fully developed eddy field predicted by the GRB model characterize the role of mesoscale variability in the important naval problem of acoustic propagation.

THIS PAGE INTENTIONALLY LEFT BLANK

TABLE OF CONTENTS

LIST OF FIGURES

LIST OF TABLES

THIS PAGE INTENTIONALLY LEFT BLANK

LIST OF ACRONYMS AND ABBREVIATIONS

ACC	Antarctica Circumpolar Current
DoD	Department of Defense
EB	Eastward background flow
EOS	Equation of state
GDEM	Generalized Digital Environmental Model
GRB	Growth Rate Balance model
HPCMP	High Performance Computing Modernization Program
LEDPs	Large-Scale Eddy Driven Patterns
METOC	Meteorology and Oceanography
MITgcm	Massachusetts Institute of Technology General Circulation Model
NRL	Naval Research Lab
PV	Potential vorticity
RMS	Root-Mean-Square
SSP	Sound speed profile
TACC	Texas Advanced Computing Center
TL	Transmission loss
WB	Westward background flow

THIS PAGE INTENTIONALLY LEFT BLANK

ACKNOWLEDGMENTS

All effort put into the present thesis research would have been in vain were it not by the invaluable orientation of my advisor, Dr. Timour Radko. His pedagogical skills thoroughly trained me in the challenging environment of understanding fluid dynamics through numerical modeling of the ocean. I feel honored to have been working with him for the last fourteen months.

No less pleasant was to work side by side with was Dr. Jason Flanagan. All knowledge about numerical modeling implementation that I built from scratch throughout this process was definitely based upon his permanent assistance.

My quest for naval significance in my work found an end on the precise guidance of Prof. John Joseph. His field experience and acoustic expertise are impressive.

I am deeply thankful to the Brazilian Navy for believing in my potential and providing me with this lifetime opportunity of living abroad and studying in this world-class Graduate School.

Although my personal dedication guided by these fine gentlemen brought me here, I consider myself a fortunate person by joining the best METOC group ever: Jim, Mary, David D., David Z., Jeff, Brian and Fritz will always live in my best memories.

Last, but not less important than all people mentioned above, a profound recognition has to be delivered to my family. Fernanda and Arthur are the angels that were sent to my life to protect me against all odds. All patience they exercised during these twenty-seven months will not be forgotten. I shall include in this group Carlos, Guillermo, Ricardo, Renato, Roger's and Paulo's friendly families. You are part of my family now.

This work was supported in part by a grant of computer time from the Department of Defense High Performance Computing Modernization Program (DoD HPCMP). I also acknowledge the Texas Advanced Computing Center (TACC) at the University of Texas at Austin for providing HPC and visualization resources that have contributed to the research results reported within this thesis.

THIS PAGE INTENTIONALLY LEFT BLANK

I. INTRODUCTION

A. MESOSCALE VARIABILITY

In basic general circulation classes, the first step oceanographers take after writing the governing equations is to replace the total fields with their mean values. However, such a necessary simplification could lead to the misleading perception that ocean flows are laminar rather than turbulent. In reality, mesoscale eddies are all over the ocean as shown in Figure 1. Eddies vary in appearance, but can be viewed simply as variability around a mean (background) flow. Such variations are observable over areas of thousands of square kilometers and last for weeks or months (Robinson 1983).

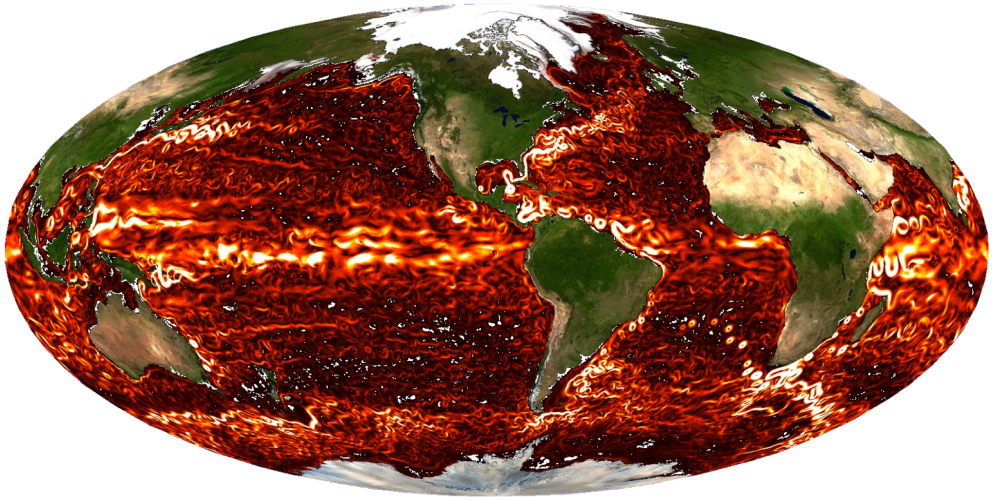

Figure 1. Global scale representation of the general ocean circulation. From ECCO2/JPL/NASA Project, 2004. Image available from ECCO2 at http://ecco2.jpl.nasa.gov/animations.

Eddies are important because they transport ocean properties—heat, salt and oxygen, for instance—through the so-called eddy-induced fluxes. The importance of mesoscale eddies cannot be overstated. For example, the Meridional Overturning Circulation is reinforced in turbulent regions like the Antarctica Circumpolar Current (ACC) and greatly impacts global climate changes (Wolfe and Cessi 2010, 2011; Radko and Kamenkovich 2011). Another example is the effect of eddies on the structure of the

thermocline (Rhines and Young 1982; Radko and Marshall 2004; Henning and Vallis 2005) that in turn impacts acoustic propagation. One of the most striking examples of eddy-induced fluxes is the heat transport by the Gulf Stream (Figure 2). Very sharp gradients of temperature induce detachment of warm core eddies from the north wall of the Gulf Stream, and cold core eddies from its southern boundary into the Sargasso Sea. As a result, the amount of heat transferred by the Gulf Stream from the tropics to the high latitudes is substantially increased relative to the mean transport.

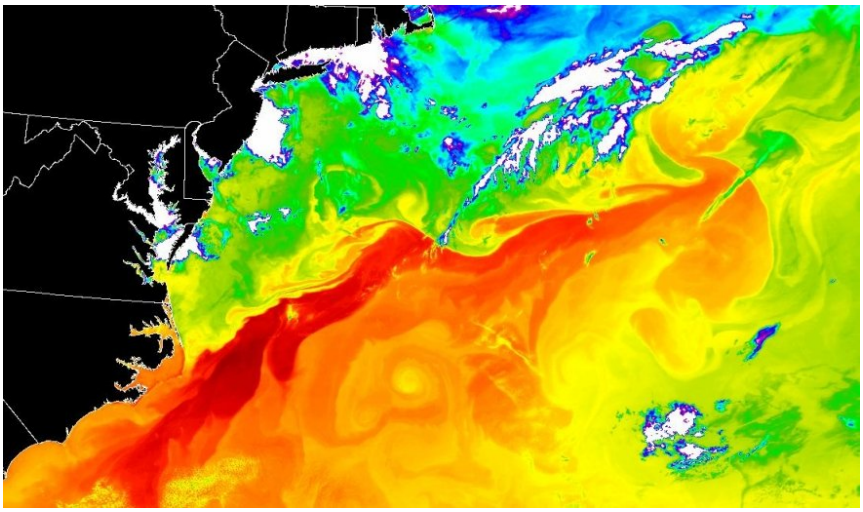

Figure 2. Gulf Stream meandering along the East Coast of the United States. From SSEC EOS Direct Broadcast, 2007. Image available from OceanMotion.org at http://oceanmotion.org/html/impact/climate-variability.htm.

Although the significance of eddy-induced fluxes in the global ocean is firmly established, the actual physics behind the development and equilibration of instabilities leading to generation of eddies is still poorly understood. The nonlinear character of mesoscale variability makes it difficult to predict eddy-induced fluxes and a general theory of eddy-induced transport is still missing. Researchers typically attempt to formulate physically based parameterizations to predict the evolution of tracer fields in coarse resolution models. The classic approach to the representation of eddy-induced mixing has been through parameterization since the available coarse resolution climate models do not provide adequate spatial resolution (Gent and McWilliams 1990; Visbeck et al. 1997; Eden 2011). The most common solution is to introduce a uniform, in space

and in time, eddy diffusivity coefficient. However, the current generation of eddy parameterizations introduces uncertainties in the prediction of quantities, such as the amount of pole-ward heat transport. A reliable theoretical model that explains eddy dynamics could greatly advance our ability to represent eddies in coarse resolution models.

B. BACKGROUND

Recent improvements in computational resources have allowed for the use of eddy-resolving numerical models (Lévy et al. 2010) to produce variability and assess its mixing effects. Therefore, the physics of eddy development and their effects on tracer distributions can now be more thoroughly described using fine resolution models. Several models focus on baroclinic instabilities (since they are a primary source of eddy kinetic energy). Analytical models, on the other hand, often utilize linear instability theory to explain how instabilities grow from initial perturbations (Charney 1947; Eady 1949; Phillips 1951) but do not show how the equilibration of eddy-induced fluxes is achieved as observed in nature. Others utilize weakly nonlinear models (Pedlosky 1970, 1971, 1981) to compute equilibrated fluxes but fail to explain the dynamics of large-amplitude eddies. Models based on scaling laws (Larichev and Held 1995; Held and Larichev 1996; Frisius 1998; Lapayere and Held 2003; Thompson and Young 2006, 2007) analyze eddy-induced transports at different scales, but their applicability depends on the reference scales. Phenomenological models examine eddy-induced transport by considering regular arrays of eddies, and assessing their cumulative effect on the general circulation (Spall and Chapman 1998; Manfroi and Young 1999, 2002; Novikov and Papanicolaou 2001; Radko 2011, 2012). However, the predictions of such models have not been sufficiently general or consistent.

The limitations of these previous attempts could be addressed through the analysis of the actual dynamics of eddy development. First, the growth of instabilities could be linked to measurable parameters of the background flow. Second, the equilibration level could be predicted based on a growth rate balance discussed in the next section. Third, it would be possible to perform a spectral decomposition of the transport to study the

relevant interactions between mesoscale eddies and Large-Scale Eddy-Driven Patterns (LEDPs). Once insight into the pattern, quantification, and spectral composition of mesoscale variability is established, it is possible to produce a model to predict the development of its dependences on the stratification, depth, and shear of the background current.

C. THE GROWTH RATE BALANCE MODEL

This study focuses on a theoretical method to explain the development and equilibration of mesoscale variability as a competition between primary and secondary instabilities. In a baroclinically unstable ocean, initial perturbations in the vertical shear of the horizontal flow cause the amplitude of instabilities to grow in time. The fastest growing modes (primary modes) are oriented in the meridional direction, as indicated in Figure 3a. The growth of secondary instabilities takes longer, but their amplitudes eventually become larger than the primary mode amplitudes. At this point, the pure meridional modes are disrupted by sinusoidal modes that contain significant zonal variability (see Figure 3b).

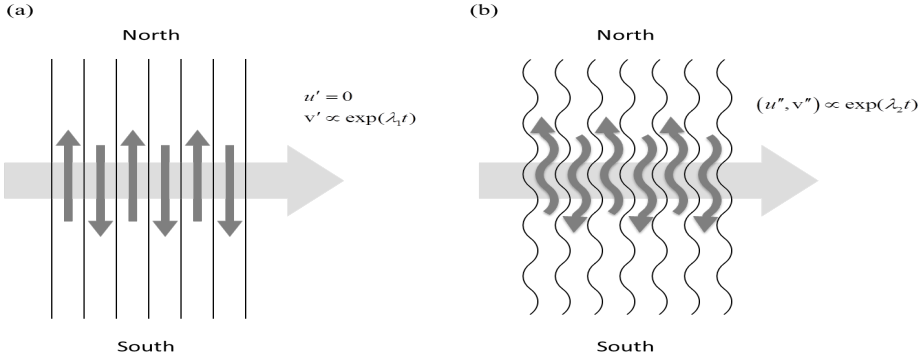

Figure 3. Schematic of primary (left) and secondary instabilities (right).

Both the primary and secondary mode growth rates depend on background parameters (vertical shear, beta-effect, bottom drag, and stratification). However, the growth rate of secondary instabilities also depends on the amplitude of the primary instabilities. The dynamics of primary and secondary instabilities are linked through a linear balance given by a coefficient *C* of order one, given by

$$\lambda_2 = C\lambda_1 \tag{1}$$

where the indices 1, 2 indicate primary, secondary modes, and λ is the growth rate. As a result, the coefficient *C* can be regarded as the parameter that determines the amplitude of equilibrated baroclinic instabilities. The underlying physics of this relationship are determined by the monotonic dependence of λ_2 on the amplitude of the primary modes. When the amplitude of the primary modes is too small, the growth rate of the secondary modes remains relatively small. As the amplitude of the primary mode increases, it pumps up the secondary mode growth rate. As a result, the secondary instabilities gain in magnitude, rapidly reaching the level of primary modes, and suppress their growth. At this stage, the system reaches statistical equilibrium.

An algorithm, based on the GRB assumption, is employed to evaluate the amplitude of equilibrated baroclinic waves. The algorithm first assumes a value for the coefficient *C* (the correct value is not defined by the GRB, but it is later refined through simulations). Linear instability theory is then used to determine the linear growth of primary instabilities. The Floquet theory for the stability of boundary layer flows (Herron 1984) is next invoked to compute the growth rate of secondary instabilities based on the amplitude of the primary instabilities. These two steps are computed in a Maple code that verifies if the value for λ_2 satisfies the growth rate balance (1). If not, then the Maple code iterates until the balance is satisfied. Typically, 10 to 11 iterations are needed to satisfy the balance to within an error of magnitude 10^{-5}. The final step is to use the equilibrated amplitude to compute variability statistics like potential vorticity (PV) or heat fluxes. Two configurations are utilized to validate the algorithm. The first is a simple two-layer model that solves the Phillips problem (Phillips 1951). The second is a more realistic configuration that solves the Eady problem (Eady 1949) in a continuously

stratified model. In the latter, the Eady system is solved for the root-mean-square (RMS) velocities profiles and compared to a simulation performed with the Massachusetts Institute of Technology General Circulation Model (MITgcm) (Marshall et al. 1997a, b).

D. ORGANIZATION

This thesis is focused on the growth rate balance model, which is applied to two configurations of baroclinically unstable models. A two-layer numerical model is compared to the Phillips problem of general circulation in Chapter II. Scale interactions between large-scale features and mesoscale eddies observed during the experiments motivate Chapter III. A three-dimensional model is compared to the Eady problem of a continuously stratified model in Chapter IV. Chapter V presents an analysis of acoustic signatures in fully developed mesoscale eddy fields. Finally, Chapter VI summarizes all findings, and Chapter VII suggests future research that could follow this study.

II. EDDY-INDUCED TRANSPORT IN A TWO-LAYER MODEL

Mesoscale variability can be a result of i) interaction of the flow with topography, ii) lateral shear of the flow (barotropic instability) and iii) vertical shear of the flow (baroclinic instability). This thesis focuses on baroclinic instability as the source of mesoscale variability. Fluxes are evaluated from an unstable two-layer quasi-geostrophic model and compared with the equilibrated fluxes predicted by an algorithm based on the GRB assumptions. The Phillips problem (Phillips 1951) represents the baroclinically unstable flow by two layers of homogeneous and incompressible fluids of different densities. The adopted model in Figure 4 is generally based on the two-layer quasi-geostrophic model (Pedlosky 1987). Baroclinic instability is created by setting up an upper layer with a zonal background flow U and a motionless lower layer. However, the developing instabilities lead to finite-amplitude motions in both upper and lower layers. Potential vorticity (PV) is the tracer of interest since it is readily available from the GRB model for the Phillips configuration. However, it should be mentioned that the differences between PV fluxes and passive tracer fluxes are generally small, less than 10%. This result is detailed in Section C.

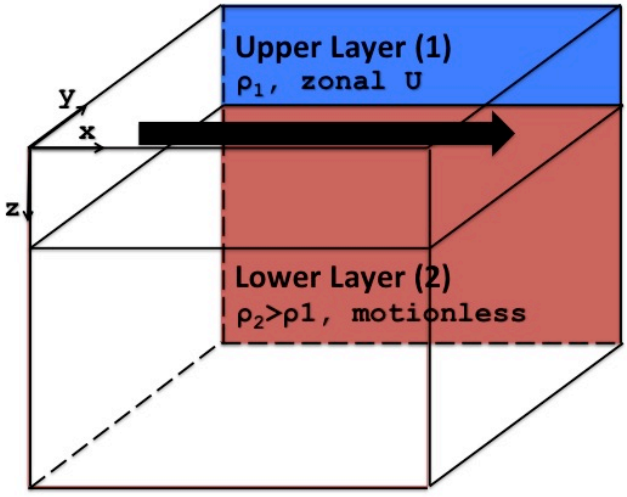

Figure 4. Schematic of the two-layer model.

A. NUMERICAL MODEL DESCRIPTION

1. Governing Equations

The numerical model computes the flow evolution in the Phillips configuration with a spectral method similar to the one used in Radko and Stern (1999). The two-layer quasi-geostrophic equations (e.g., Pedlosky 1987) solved are

$$\frac{\partial Q_1}{\partial t} + J(\Psi_1, Q_1) = \nu \nabla^4 \Psi_1 \tag{2}$$

$$\frac{\partial Q_2}{\partial t} + J(\Psi_2, Q_2) = \nu \nabla^4 \Psi_2 - \gamma \nabla^2 \Psi_2 \tag{3}$$

$$Q_1 = \nabla^2 \Psi_1 + \frac{f^2}{g' H_1}\left(\Psi_2 - \Psi_1\right) + \beta y \tag{4}$$

$$Q_2 = \nabla^2 \Psi_2 + \frac{f^2}{g' H_2}\left(\Psi_1 - \Psi_2\right) + \beta y \tag{5}$$

where each layer is represented by the streamfunction Ψ and the potential vorticity Q. Here, the subscripts 1 and 2 apply to the upper and lower layers respectively, with the thickness of each layer represented by H_1, H_2. The coefficients include the eddy viscosity ν, and the bottom drag γ. The earth's rotation is included in the model through the Coriolis parameter f and the vorticity gradient β; g' is the reduced gravity, which accounts for the density differences between the two layers.

The background flow $\overline{\Psi}$ is subtracted from the actual flow to express the governing equations in terms of the perturbations ψ. A similar treatment is applied to the perturbations of PV (q). The objective here is to assess the dependences of the equilibrated fluxes on seven background parameters. They are the background flow U, the radius of deformation in the upper layer

$$Rd_1 = \frac{1}{f}\sqrt{g' H_1} \tag{6}$$

at which the rotational effects become as relevant as buoyancy (Gill 1982), H_1, H_2, β, γ and ν. Such a large number of parameters present a major obstacle to the assessment of individual dependences. Therefore, to simplify the task, the parameters are rewritten in

non-dimensional units using Rd_1, U, and $\frac{Rd_1}{U}$ as the scales of length, velocity and time respectively. As a result, only four non-dimensional governing parameters need to be assessed:

$$\beta_{nd} = \frac{\beta Rd_1^2}{|U|} \tag{7}$$

$$r = \frac{H_1}{H_2} \tag{8}$$

$$\gamma_{nd} = \frac{\gamma Rd_1}{|U|} \tag{9}$$

$$\upsilon_{nd} = \frac{\nu}{Rd_1|U|} \tag{10}$$

where β_{nd} is the non-dimensional vorticity gradient, r is the layer thickness ratio, γ_{nd} is the non-dimensional bottom drag coefficient, and ν_{nd} is the non-dimensional eddy viscosity coefficient. Dependence on viscosity is found to be very weak in the experiments, so this leaves only three relevant dependences to evaluate.

The numerical model solves the non-dimensional equations

$$\frac{\partial q_1}{\partial t} + J(\psi_1, q_1) + (\beta_{nd} + s)\frac{\partial \psi_1}{\partial x} + s\frac{\partial q_1}{\partial x} = \nu_{nd}\nabla^4\psi_1 \tag{11}$$

$$\frac{\partial q_2}{\partial t} + J(\psi_2, q_2) + (\beta_{nd} - sr)\frac{\partial \psi_2}{\partial x} = \nu_{nd}\nabla^4\psi_2 - \gamma_{nd}\nabla^2\psi_2 \tag{12}$$

$$q_1 = \nabla^2\psi_1 + \left(\psi_2 - \psi_1\right) \tag{13}$$

$$q_2 = \nabla^2\psi_2 + r\left(\psi_1 - \psi_2\right) \tag{14}$$

where

$$s = \frac{U}{|U|} \tag{15}$$

indicates Westward background flows (WB) if negative, or Eastward background flows (EB) if positive. The passive tracer perturbations c' are computed through

$$\frac{\partial c_1'}{\partial t} + J(\psi_1, c_1') + \frac{\partial \psi_1}{\partial x} + \frac{\partial c_1'}{\partial x} = \nu_{nd}\nabla^2 c_1' \tag{16}$$

$$\frac{\partial c_2'}{\partial t} + J(\psi_2, c_2') + \frac{\partial \psi_2}{\partial x} = \nu_{nd} \nabla^2 c_2' \tag{17}$$

to verify the aforementioned less than 10% flux difference and justify the PV fluxes as representative variability statistics.

2. Model Configuration

A typical set of governing parameters used in this study, representative of typical large-scale flows in the ocean interior (Talley et al. 2011), is given by $U = 0.05$ ms^{-1}, $Rd_1 = 25$ km, $\beta_{nd} = 0.25$ (from $\beta = 2 \times 10^{-11}$ m^{-1}s^{-1}), $r = 1/3$ (from $H_1 = 1$ km and $H_2 = 3$ km), $\gamma_{nd} = 0.5$ (from $\gamma = 10^{-6}$ s^{-1}) and $\nu_{nd} = 0.005$ (from $\nu = 10$ m^{2}s^{-1}). These values are varied in further simulations. In what follows, the term "large domain" refers to the doubly periodic domain that extends 3750 km in the zonal direction (allowing at least 20 mesoscale eddies to align) and 1875 km in the meridional direction (allowing at least 10 waves to propagate in parallel). The grid spacing is 2.5 km allowing for the full resolution of mesoscale eddies.

The analyses of equilibrated eddy-induced flux dependences on β_{nd} and r conducted in this chapter are derived from the initial basic configuration. The dependences on γ_{nd} are more complex. As γ_{nd} is decreased, there is increasing development of large-scale features referred to as Large-Scale Eddy Driven Patterns (LEDPs). In such LEDP-dominant regimes, the GRB fails to predict equilibration. Hence, this analysis is postponed to Chapter III. To preclude the existence of large-scale features from equilibrated eddy fields, a doubly periodic domain that extends 500 km in each lateral direction is also utilized. In what follows, the term "small domain" refers to this domain.

3. Model Outputs

The main outputs of the numerical model runs are the anomalies of potential vorticity, passive tracer, and flow velocity that make it possible to analyze how fluxes develop from rest. The statistics of interest are

$$V'_{nd} = \frac{\partial \psi_{nd}}{\partial x} \tag{18}$$

$$F_{qnd1} = \overline{V'_{nd1} q_1} \tag{19}$$

$$F_{qnd2} = \overline{V'_{nd2} q_2} \tag{20}$$

$$K_{qnd1} = -\frac{\overline{V'_{nd1} q_1}}{\beta_{nd} + s}, K_{cnd1} = -\overline{V'_{nd1} c'_1} \tag{21}$$

$$K_{qnd2} = -\frac{\overline{V'_{nd2} q_2}}{\beta_{nd} - sr}, K_{cnd2} = -\overline{V'_{nd2} c'_2} \tag{22}$$

describing the non-dimensional (meridional) PV fluxes F_{qnd1} , F_{qnd2} and eddy diffusivity coefficients K_{qnd1} , K_{qnd2} . The eddy diffusivity equations follow the closure for mesoscale eddy-induced fluxes described in Eden (2011) using the linear instability theory. The larger the diffusivity coefficient, the larger the average fluxes of the property, or the smoother the meridional gradient of the property. Note that positive values of flux imply that the property is being advected to the North.

B. GROWTH RATE BALANCE THEORY

1. Equilibration

Figure 5 presents a sample time record of non-dimensional PV fluxes. Initially (t_{nd} = 0) there is zero PV flux. However, tiny initial perturbations grow (t_{nd} ~ 200) as instabilities get organized in baroclinic wave modes. The equilibrium level occurs for t_{nd} > 300 and is achieved through the balance (1).

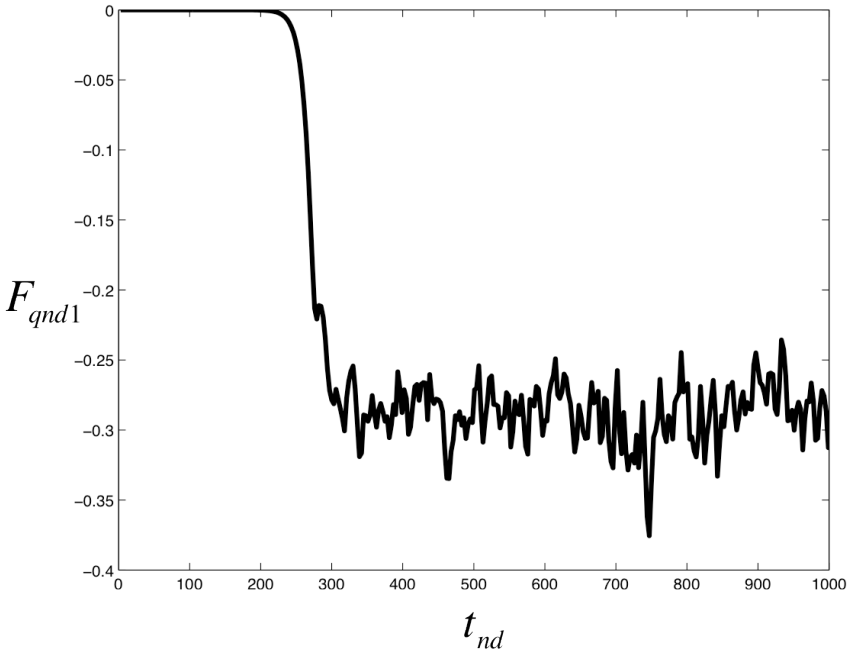

Figure 5. PV flux time series.

The perturbations of the PV field in the numerical model are presented in Figure 6, and demonstrate the instability development as predicted by the GRB model. Shown is a composition of three successive snapshots of the upper layer PV anomaly. The random initial perturbations lead to meridional wave trains as prescribed in the linear growth theory for the fastest growing instabilities. The first mode waves show up in Figure 6a ($t_{nd} \sim 250$) as nearly straight lines in the meridional direction. This pattern remains while secondary instabilities are still growing. At $t_{nd} \sim 305$ (Figure 6b) secondary instabilities have grown sufficiently strong to break the straight-line pattern. At $t_{nd} \sim 450$ (Figure 6c) equilibrium is reached, and eddies are visible throughout the entire domain.

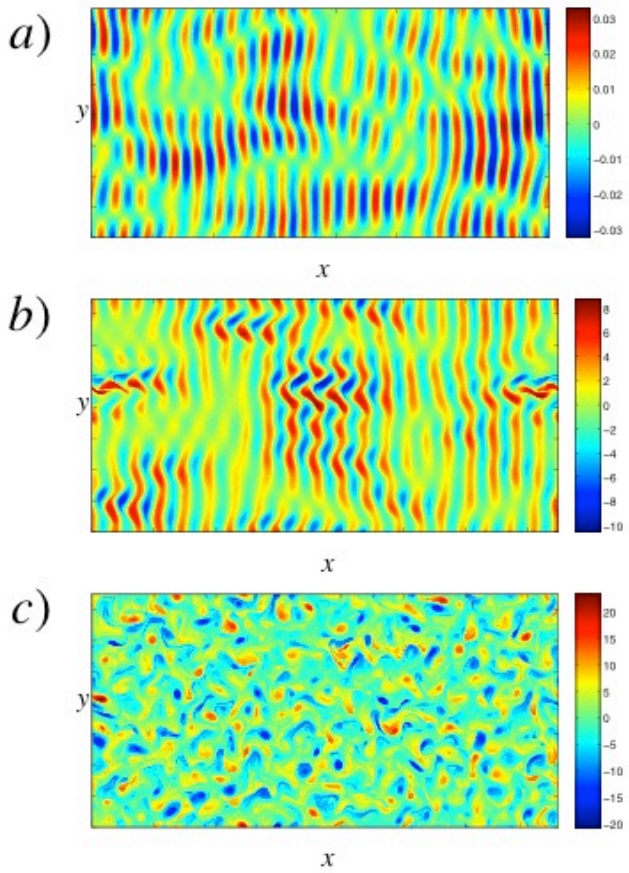

Figure 6. Snapshots of the PV anomaly field evolution in the large domain.

2. Solution Stability

In order to develop a predictive theoretical model based on the GRB assumption, the upper, lower layer streamfunction ψ_1, ψ_2, are divided into a basic state represented by the equilibrated perturbations $\tilde{\psi}_1$, $\tilde{\psi}_2$, and variations about this basic state ψ_1', ψ_2'. The basic state is represented by the primary mode solutions for each layer

$$\tilde{\psi}_1 = A_1 \cos(kx) \tag{23}$$

$$\tilde{\psi}_2 = A_2 \cos(kx + \varphi) \tag{24}$$

with upper, lower layer amplitude A_1, A_2, zonal wavenumber k, and phase shift φ between the modes that propagate in the upper and lower layers. The objective is to

determine the amplitudes A achieved by the primary instabilities when the secondary instabilities become important and lead to equilibrium following the growth rate balance theory.

If the wavenumber of the primary mode solutions were considered as k_0 (the wavenumber of the primary modes at zero growth rate), the amplitude of the primary instabilities would be constant, and the governing equations would represent a well-posed stability problem. In the numerical model, the primary modes are better represented by $k_{\max}$ (the wavenumber corresponding to the fastest growing modes). In this case, the basic state becomes time-dependent, and the problem becomes ill posed. The stability analysis of flows that depend on time is possible (Sivashinsky 1985; Manfroi and Young 2002; Balmforth and Young 2002, 2005). It includes artificial forcing in the momentum conservation to maintain the steady state—called quasi-steady state approximation (Lick 1965; Robinson 1976; Kimura and Smith 2011; Radko and Smith 2012). For this reason, $k_{\max}$ is used as the primary mode wavenumber to determine the basic state of perturbations during the equilibrium period. Therefore, the following set of equations

$$\frac{\partial q_1'}{\partial t}+\frac{\partial \tilde{\psi}_1}{\partial x}\frac{\partial q_1'}{\partial y}-\frac{\partial \psi_1'}{\partial y}\frac{\partial \tilde{q}_1}{\partial x}+(\beta_{nd}+s)\frac{\partial \psi_1'}{\partial x}+\frac{\partial q_1'}{\partial x}=\nu_{nd}\nabla^4\psi_1' \tag{25}$$

$$\frac{\partial q_2'}{\partial t}+\frac{\partial \tilde{\psi}_2}{\partial x}\frac{\partial q_2'}{\partial y}-\frac{\partial \psi_2'}{\partial y}\frac{\partial \tilde{q}_2}{\partial x}+(\beta_{nd}-sr)\frac{\partial \psi_2'}{\partial x}=\nu_{nd}\nabla^4\psi_2'-\gamma_{nd}\nabla^2\psi_2' \tag{26}$$

$$q_1'=\nabla^2\psi_1'+\left(\psi_2'-\psi_1'\right) \tag{27}$$

$$q_2'=\nabla^2\psi_2'+r\left(\psi_1'-\psi_2'\right) \tag{28}$$

adequately describe the perturbations on the basic state.

The Floquet theory is adapted to solve for the growth rate of secondary perturbations by expanding the streamfunction perturbations in Fourier harmonics as follows:

$$\left(\psi_1'\right) = \exp(if_q kx + imy + \lambda t) \sum_{n=-N}^{N} \psi_1^{(n)} \exp\left(inkx\right) \tag{29}$$

$$\left(\psi_2'\right) = \exp(if_q kx + imy + \lambda t) \sum_{n=-N}^{N} \psi_2^{(n)} \exp\left(inkx\right) \tag{30}$$

with growth rate λ, zonal and meridional wavenumbers k and m respectively, and Floquet coefficient f_q. Each mode is represented by N Fourier components. The Floquet coefficient controls the fundamental zonal wavelength. The eigenvalues of the matrix A_q

$$\lambda\vec{\xi} = A_q\vec{\xi} \tag{31}$$

represent the growth rates of the normal modes $\vec{\xi}$

$$\vec{\xi} = (\psi_1^{(-N)}, \psi_2^{(-N)}, \psi_1^{(-N+1)}, \psi_2^{(-N+1)}, ..., \psi_1^{(N)}, \psi_2^{(N)}) \tag{32}$$

as function of k, m, f_q, β_{nd}, γ_{nd}, ν_{nd}, A_1, A_2, φ, and N. The fastest growing mode corresponds to the eigenvalues of A_q with the largest real part for each input parameter set.

The secondary growth rate can now be evaluated for given β_{nd}, γ_{nd}, ν_{nd}, r, N and A_1. However, the solution for the growth rate of secondary instabilities λ_2 rapidly converges with increasing N and therefore its specific value is of secondary importance.

3. Sensitivity of Solutions to the GRB Coefficient *C*

Once the dependence of the growth rate λ_2 on the amplitude is established, the latter can be recovered from the growth rate balance (1). The growth rate of primary instabilities λ_1 can be computed using linear instability theory for a chosen set of input parameters β_{nd}, γ_{nd}, ν_{nd}, r. However, the exact value of the coefficient C is not known and therefore the sensitivity of the solutions to this coefficient is now explored. Thus, a plausible range of C is considered and, for each value, the amplitude A_1 is iteratively

computed as follows. First, an initial guess of A_1 is made. This implies a value for λ_2 that is different from the one that satisfies (1). Successive iterations adjust values for A_1, in a way that would reduce the error of (1). The procedure is repeated until the desired accuracy is achieved. Usually 10 to 11 iterations are needed to obtain the growth rate balance within an error of magnitude 10^{-5}. Finally, the amplitude of the primary instabilities A_1 determines the magnitude of the streamfunction or any other property after equilibration. The following diagnostics are based on the equilibrated PV fluxes.

The parameters β_{nd} and r are varied separately for several plausible values of C. Figure 7 shows the equilibrated PV fluxes as a function of $s\beta_{nd}$. The magnitude of fluxes is larger for small values of β_{nd}. Fluxes change sign for positive and negative values of β_{nd} with upper and lower layers fluxes having opposite signs as well. Fluxes are larger for larger values of the coefficient C.

Figure 8 shows the PV fluxes as a function of the thickness ratio, and the dependence is characterized by monotonic increase with r. In this case, fluxes also increase with C.

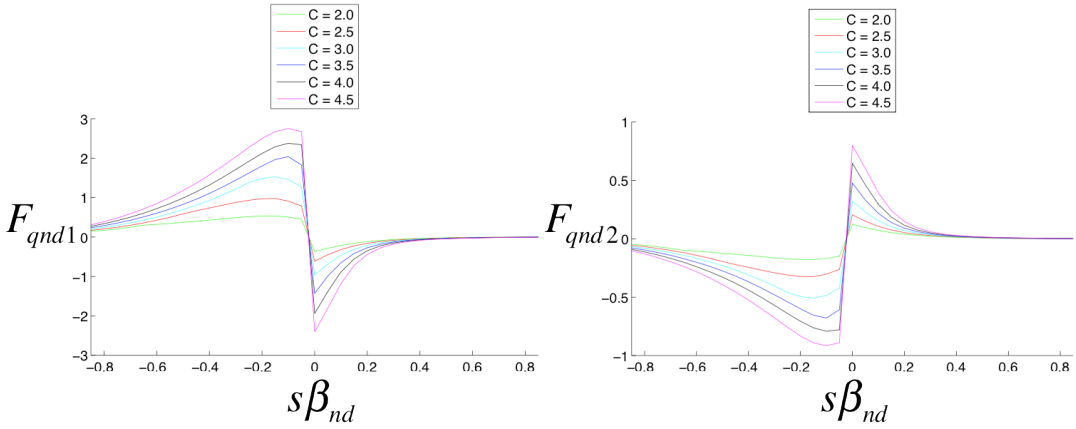

Figure 7. PV fluxes in the upper (left) and lower layers as a function of β_{nd} for different coefficient C values.

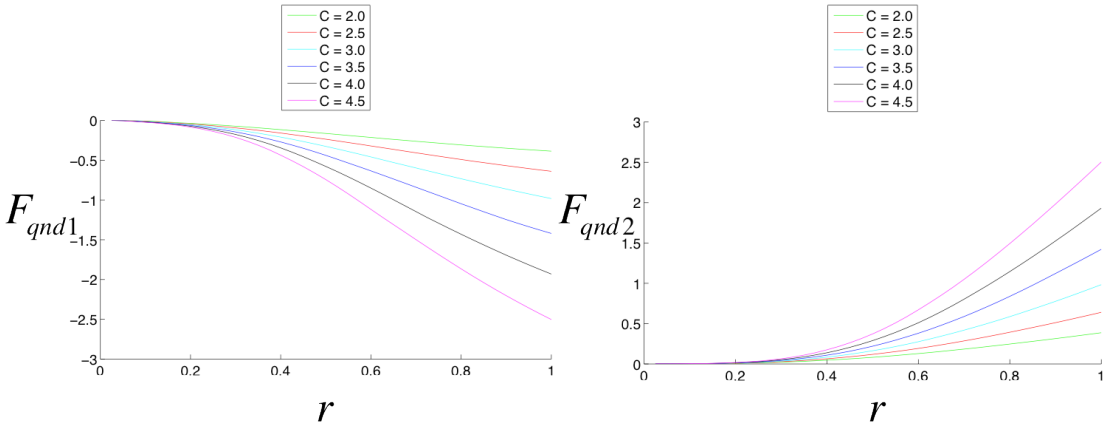

Figure 8. PV fluxes in the upper (left) and lower layers as a function of r for different coefficient C values.

C. NUMERICAL SIMULATIONS AND CALIBRATION OF THE GRB THEORY

1. Mesoscale Variability as a Function of β_{nd}

The dependence of mesoscale variability on β_{nd} is examined through 23 numerical simulations, each with a different $s\beta_{nd}$ taken from the range [-0.85, 0.85] with fixed r = 1/3. The analysis is based upon the PV fluxes time-averaged over the equilibrium period. Figures 9 through 12 show representative PV flux time series (from both layers) diagnosed from those simulations.

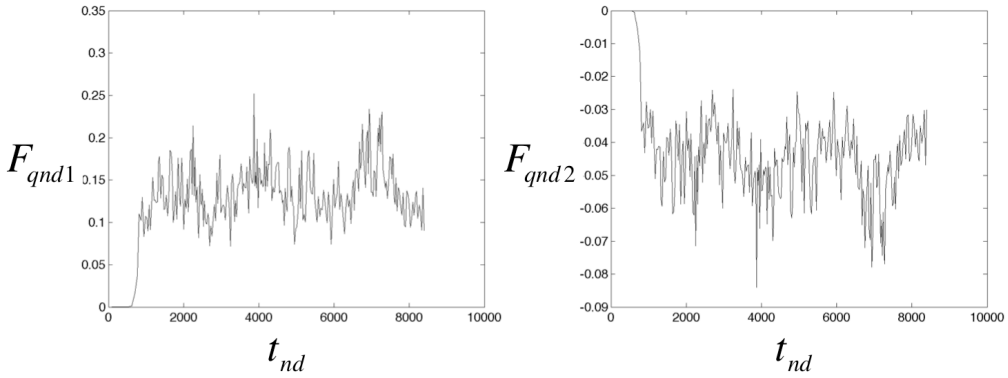

Figure 9. PV flux time series in the upper (left) and lower layers for $s\beta_{nd}$ = -0.85.

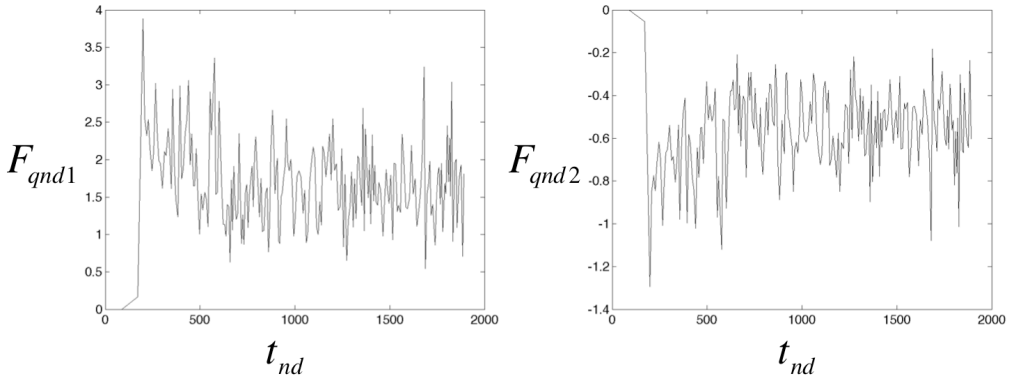

Figure 10. PV flux time series in the upper (left) and lower layers for $s\beta_{nd}$ = -0.25.

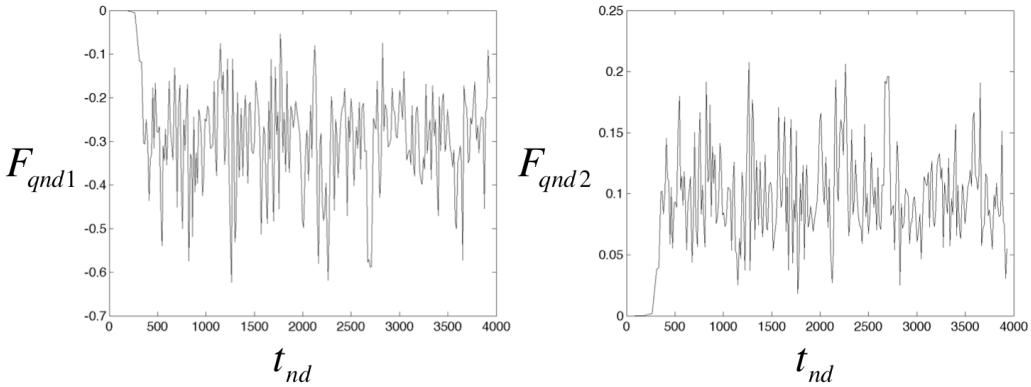

Figure 11. PV flux time series in the upper (left) and lower layers for $s\beta_{nd}$ = 0.25.

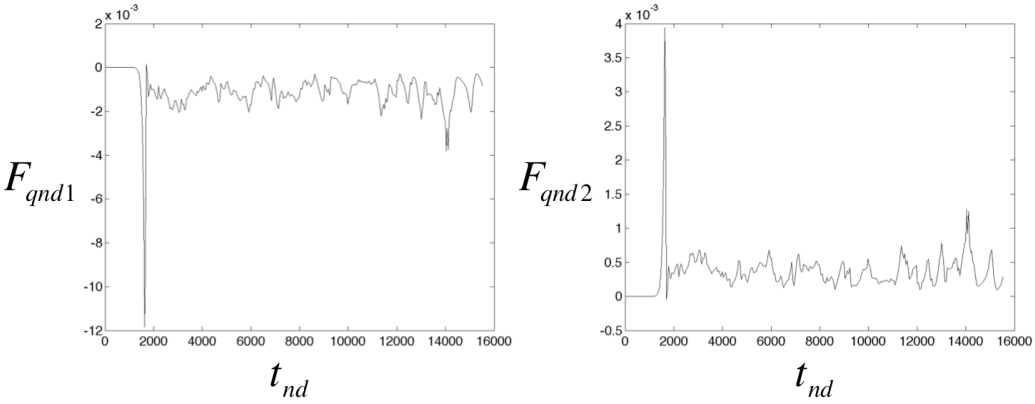

Figure 12. PV flux time series in the upper (left) and lower layers for $s\beta_{nd}$ = 0.85.

Equilibrium is reached at different times and with different magnitudes and directions for each value of $s\beta_{nd}$. Simulations with small values of β_{nd} equilibrate faster due to much higher primary growth rates. WB flows equilibrate faster than EB with the same value of β_{nd}. This observation agrees with Kamenkovich et al. (2009) that describe WB flows as less stable. The transport of PV by eddies is to the South (negative values) in the upper layer for negative values of $s\beta_{nd}$, but in the opposite direction in the lower layer. The opposite behavior is observed for positive values of $s\beta_{nd}$. Simulations with negative values of $s\beta_{nd}$ equilibrate with larger magnitudes of PV fluxes than their positive counterparts. In general, there is a monotonic increase in PV fluxes as the value of β_{nd} decreases towards zero—smaller values of β_{nd} correspond to stronger background flows or shorter radii of deformation. Table 1 contains the values of PV fluxes and diffusivity coefficients for each layer, as diagnosed from each of the 23 numerical simulations.

$s\beta_{nd}$	F_{qnd1}	K_{qnd1}	F_{qnd2}	K_{qnd2}
-0.8500	0.1382	0.9211	-0.0461	0.0389
-0.7500	0.3481	1.3924	-0.1160	0.1071
-0.6500	0.5354	1.5298	-0.1785	0.1815
-0.5000	1.0869	2.1737	-0.3623	0.4348
-0.4000	1.2426	2.0710	-0.4142	0.5648
-0.3500	1.6874	2.5960	-0.5625	0.8232
-0.3000	1.5725	2.2464	-0.5242	0.8277
-0.2500	1.7048	2.2731	-0.5683	0.9742
-0.2000	1.8685	2.3356	-0.6228	1.1679
-0.1250	2.1758	2.4866	-0.7253	1.5825
-0.0625	2.5672	2.7383	-0.8557	2.1620
-0.0375	2.2935	2.3829	-0.7645	2.0618
-0.0125	2.1026	2.1293	-0.7009	2.0268
0.0000	-1.9842	1.9842	0.6614	1.9844
0.0125	-1.6157	1.5958	0.5386	1.6789
0.0375	-1.6268	1.5680	0.5423	1.8333
0.0625	-1.3306	1.2523	0.4435	1.6379
0.1250	-0.7637	0.6788	0.2546	1.2221
0.2000	-0.4230	0.3525	0.1410	1.0577
0.2500	-0.3042	0.2434	0.1014	1.2174
0.3000	-0.2046	0.1574	0.0682	2.0478
0.3500	-0.1394	0.1033	0.0465	-2.7825
0.4000	-0.1140	0.0815	0.0380	-0.5699
0.5000	-0.0826	0.0550	0.0275	-0.1651
0.6500	-0.0015	0.0009	0.0005	-0.0016
0.7500	-0.0013	0.0007	0.0004	-0.0010
0.8500	-0.0011	0.0006	0.0004	-0.0007

Table 1. PV fluxes and diffusivity coefficients for both layers evaluated for each simulation varying β_{nd}.

The lower layer transport characteristics are more counterintuitive. Note that K_{qnd2} depends on *r,* which can lead to a singularity in K_{qnd2} for β_{nd} comparable to *r*. Lower layer fluxes assume negative values for simulations with β_{nd} greater than r.

In addition to the analysis of PV—an active tracer—it is also of interest to examine dynamics of passive tracers in the model. The passive tracer is integrated in time using (16) and (17); Figures 13 and 14 compare its meridional diffusivities with the corresponding PV diffusivities. Potential vorticity and passive tracer diffusivities are in good agreement for the upper layer, but not so much for the lower layer due to the action of the bottom drag, which directly affects the PV dynamics but not the passive tracer. Passive tracers have higher diffusivity than active tracers, but the overall difference is less than 10%. Potential vorticity acts like an active tracer in the sense that it impacts the streamfunction through the governing equations. The values obtained for active and passive tracer fluxes and diffusivity coefficients for the upper layer are given in Table 2. Note that the diffusivity difference can increase dramatically for β_{nd} around 0.85 or higher; this is a regime in which the flow becomes only weakly unstable and unlikely to become fully turbulent.

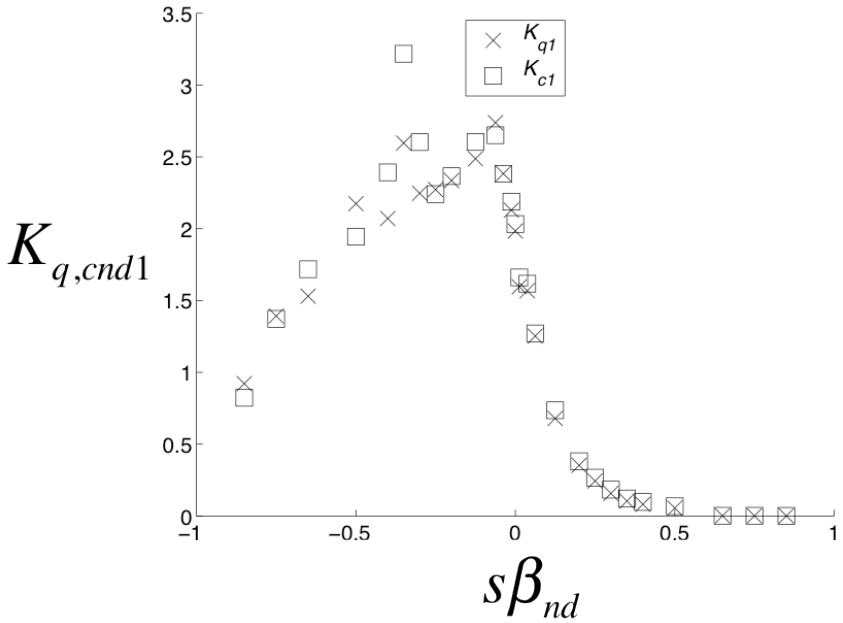

Figure 13. Comparison between PV and passive tracer diffusivities for simulations varying $s\beta_{nd}$ in the upper layer.

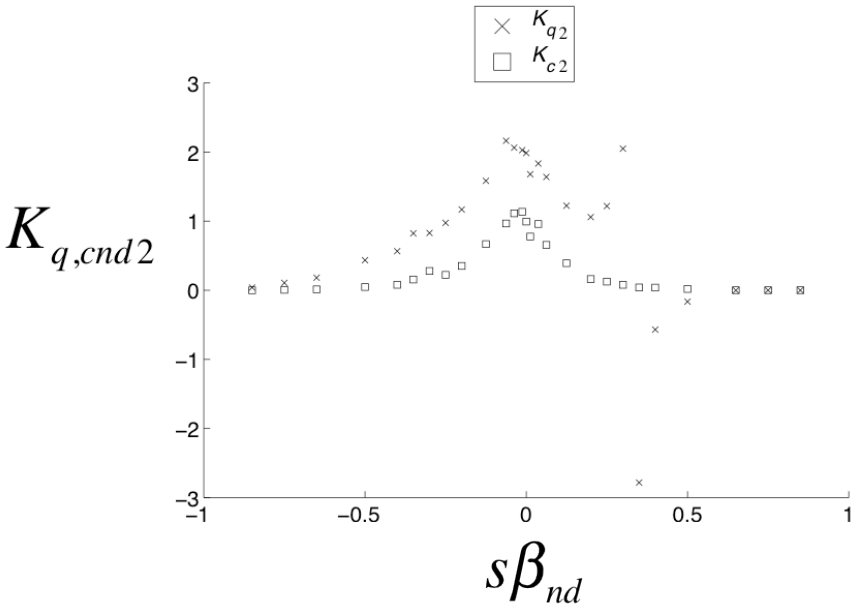

Figure 14. Comparison between PV and passive tracer diffusivities for simulations varying $s\beta_{nd}$ in the lower layer.

$s\beta_{nd}$	F_{qnd1}	K_{qnd1}	F_{cnd1}	K_{cnd1}	$(K_{cnd1}-K_{qnd1})/K_{qnd1}$
-0.8500	0.1382	0.9211	-0.8230	0.8230	-10.7%
-0.7500	0.3481	1.3924	-1.3722	1.3722	-1.5%
-0.6500	0.5354	1.5298	-1.7177	1.7177	12.3%
-0.5000	1.0869	2.1737	-1.9445	1.9445	-10.5%
-0.4000	1.2426	2.0710	-2.3920	2.3920	15.5%
-0.3500	1.6874	2.5960	-3.2174	3.2174	23.9%
-0.3000	1.5725	2.2464	-2.6030	2.6030	15.9%
-0.2500	1.7048	2.2731	-2.2406	2.2406	-1.4%
-0.2000	1.8685	2.3356	-2.3659	2.3659	1.3%
-0.1250	2.1758	2.4866	-2.6040	2.6040	4.7%
-0.0625	2.5672	2.7383	-2.6511	2.6511	-3.2%
-0.0375	2.2935	2.3829	-2.3822	2.3822	0.0%
-0.0125	2.1026	2.1293	-2.1881	2.1881	2.8%
0.0000	-1.9842	1.9842	-2.0329	2.0329	2.4%
0.0125	-1.6157	1.5958	-1.6607	1.6607	4.1%
0.0375	-1.6268	1.5680	-1.6170	1.6170	3.1%
0.0625	-1.3306	1.2523	-1.2710	1.2710	1.5%
0.1250	-0.7637	0.6788	-0.7360	0.7360	8.4%
0.2000	-0.4230	0.3525	-0.3811	0.3811	8.1%
0.2500	-0.3042	0.2434	-0.2667	0.2667	9.6%
0.3000	-0.2046	0.1574	-0.1835	0.1835	16.6%
0.3500	-0.1394	0.1033	-0.1219	0.1219	18.0%
0.4000	-0.1140	0.0815	-0.0973	0.0973	19.4%
0.5000	-0.0826	0.0550	-0.0676	0.0676	22.8%
0.6500	-0.0015	0.0009	-0.0015	0.0015	60.4%
0.7500	-0.0013	0.0007	-0.0013	0.0013	72.1%
0.8500	-0.0011	0.0006	-0.0011	0.0011	86.2%

Table 2. PV and passive tracer fluxes and diffusivity coefficients for the upper layer evaluated for each simulation varying β_{nd}.

2. Calibration of the GRB Theory Based on Variable β_{nd} Simulations

Potential vorticity fluxes recorded in the foregoing experiments are now used to determine the GRB coefficient *C*. Figures 15 and 16 plot the PV fluxes as a function of $s\beta_{nd}$ for the upper and lower layer correspondingly. These figures also include the theoretical prediction based on the GRB theory for $C = 3.5$ and $C = 4$. PV fluxes show good agreement in both layers between the analytical solutions of the theoretical model and the solutions of the numerical model. For this evaluation, 27 simulations using the

small domain are included. Based on this set of experiments, it is suggested that the relevant values of the coefficient C fall between 3.5 and 4.

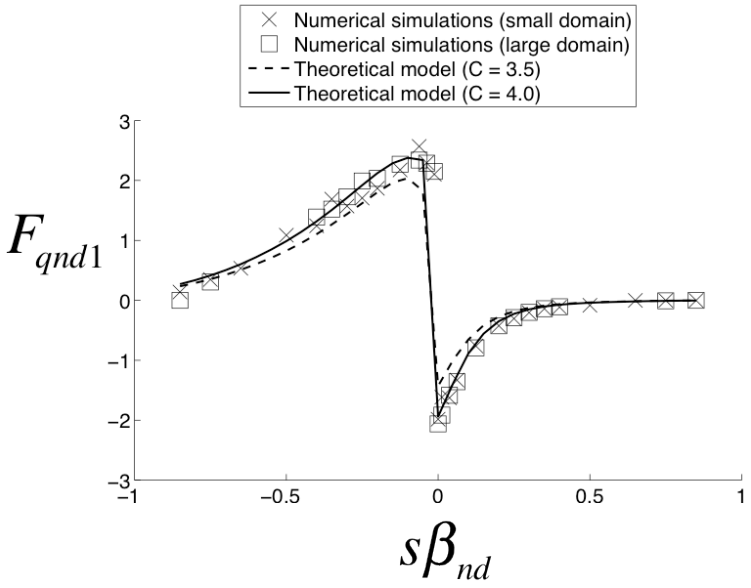

Figure 15. PV flux comparison showing best coefficient C fit for simulations varying $s\beta_{nd}$ in the upper layer.

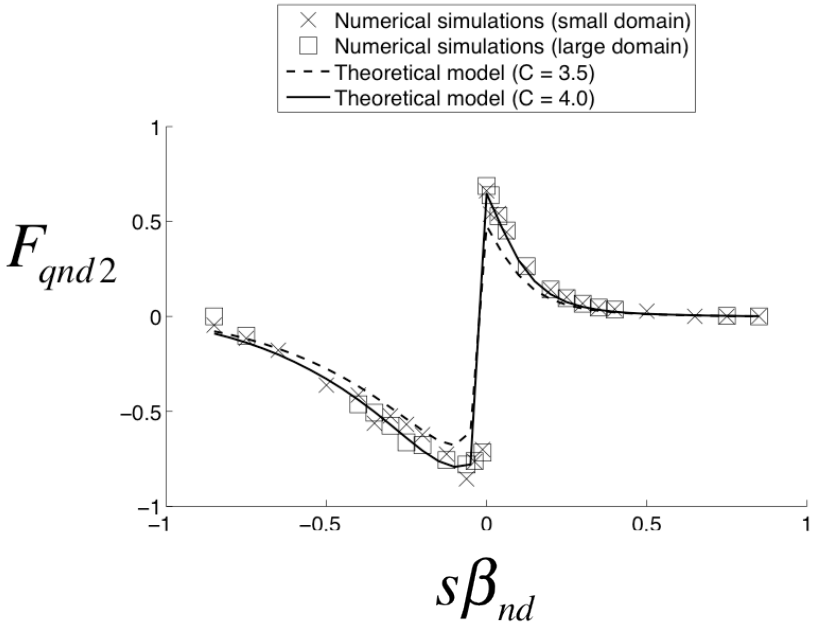

Figure 16. PV flux comparison showing best coefficient C fit for simulations varying $s\beta_{nd}$ in the lower layer.

3. Mesoscale Variability as a Function of *r*

The dependence of mesoscale variability on *r* is examined through 11 numerical simulations, each with a different *r* taken from the range [0.1, 1] with fixed β_{nd} = 0.25. The variability analysis is again based upon the average PV fluxes during the equilibrium period. Figures 17 through 20 show representative PV flux time series (from both layers) taken from these simulations.

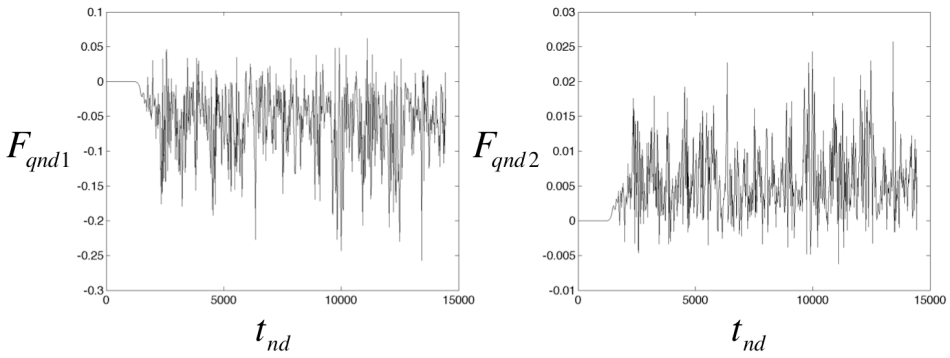

Figure 17. PV flux time series in the upper (left) and lower layers for *r* = 0.1.

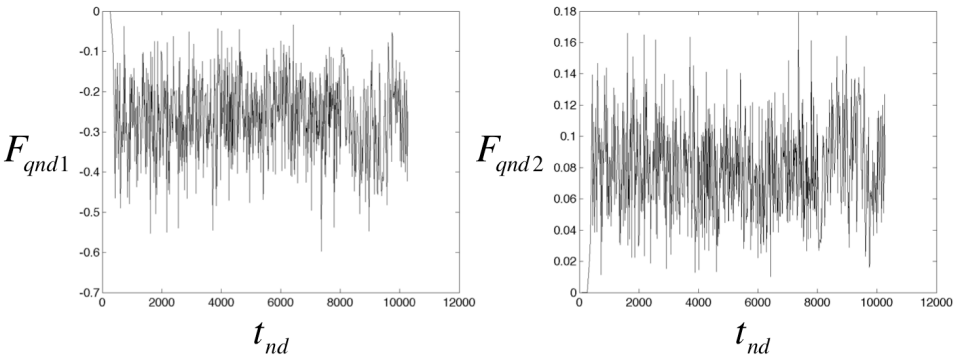

Figure 18. PV flux time series in the upper (left) and lower layers for *r* = 0.3.

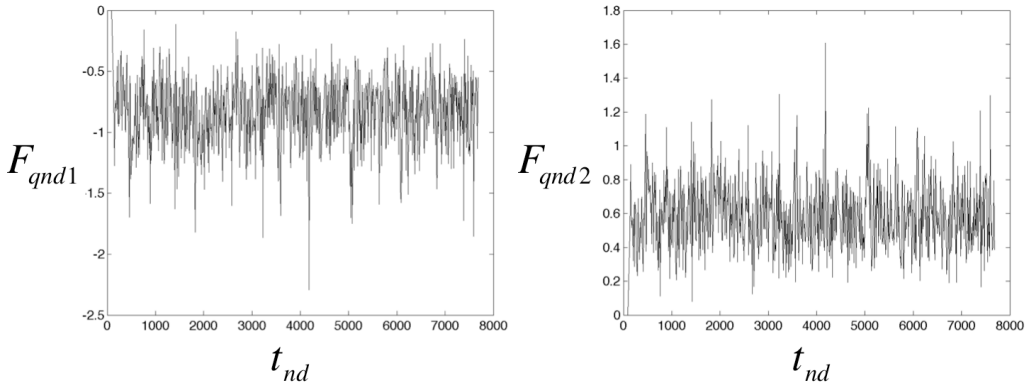

Figure 19. PV flux time series in the upper (left) and lower layers for $r = 0.7$.

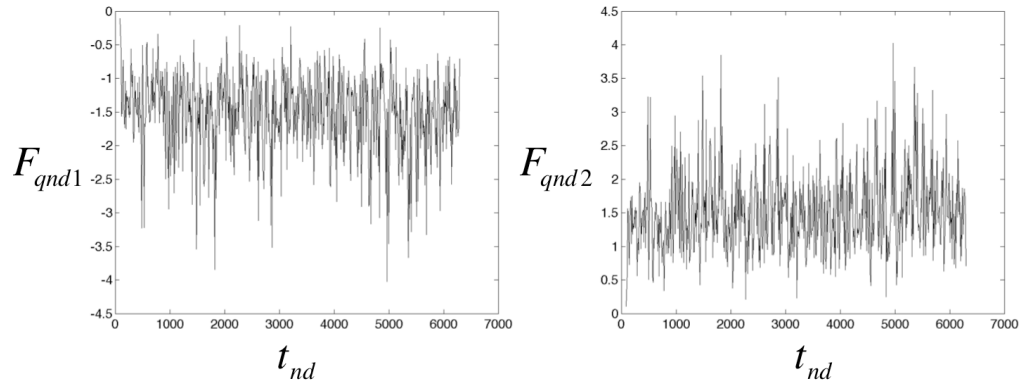

Figure 20. PV flux time series in the upper (left) and lower layers for $r = 1$.

Eddy-induced PV fluxes increase when the thicknesses of the layers become comparable. This suggests that lower layers that are much thicker than the upper layer produce less turbulence in the upper layer. This result can be rationalized based on the linear instability theory, which suggests that the growth rates rapidly reduce with decreasing r. Table 3 contains the values of PV fluxes and diffusivity coefficients for each layer.

r	F_{qnd1}	K_{qnd1}	F_{qnd2}	K_{qnd2}
0.1000	-0.0593	0.0474	0.0059	-0.0395
0.2000	-0.1576	0.1261	0.0315	-0.6305
0.3000	-0.2622	0.2098	0.0787	1.5735
0.3333	-0.2954	0.2363	0.0985	1.1821
0.4000	-0.3712	0.2970	0.1485	0.9899
0.5000	-0.5373	0.4299	0.2687	1.0747
0.6000	-0.6797	0.5438	0.4078	1.1653
0.7000	-0.8431	0.6745	0.5902	1.3115
0.8000	-1.0531	0.8424	0.8424	1.5316
0.9000	-1.2804	1.0243	1.1524	1.7729
1.0000	-1.5060	1.2048	1.5060	2.0080

Table 3. PV fluxes and diffusivity coefficients for both layers evaluated for each simulation varying *r*.

The comparison of active (PV) and passive tracer diffusivities for the variable *r* simulations confirms the results found for varying β_{nd}. The values obtained for fluxes and diffusivity coefficients for the upper layer are given in Table 4. Figure 21 confirms that in general, passive tracers have higher diffusivity than active tracers—approximately 9% greater. However, this fraction increases as the upper layer becomes much thinner than the lower layer. The lower layer diffusivities of PV differ from the corresponding passive tracer diffusivities (not shown), which mirrors the results for simulations with varying β_{nd}.

r	F_{qnd1}	K_{qnd1}	F_{cnd1}	K_{cnd1}	$(K_{cnd1} - K_{qnd1}) / K_{qnd1}$
0.1000	-0.0593	0.0474	-0.0637	0.0637	34.3%
0.2000	-0.1576	0.1261	-0.1480	0.1480	17.4%
0.3000	-0.2622	0.2098	-0.2322	0.2322	10.7%
0.3333	-0.2954	0.2363	-0.2581	0.2581	9.2%
0.4000	-0.3712	0.2970	-0.3193	0.3193	7.5%
0.5000	-0.5373	0.4299	-0.4540	0.4540	5.6%
0.6000	-0.6797	0.5438	-0.5676	0.5676	4.4%
0.7000	-0.8431	0.6745	-0.6988	0.6988	3.6%
0.8000	-1.0531	0.8424	-0.8680	0.8680	3.0%
0.9000	-1.2804	1.0243	-1.0512	1.0512	2.6%
1.0000	-1.5060	1.2048	-1.2311	1.2311	2.2%

Table 4. PV and passive tracer fluxes and diffusivity coefficients for the upper layer evaluated for each simulation varying r.

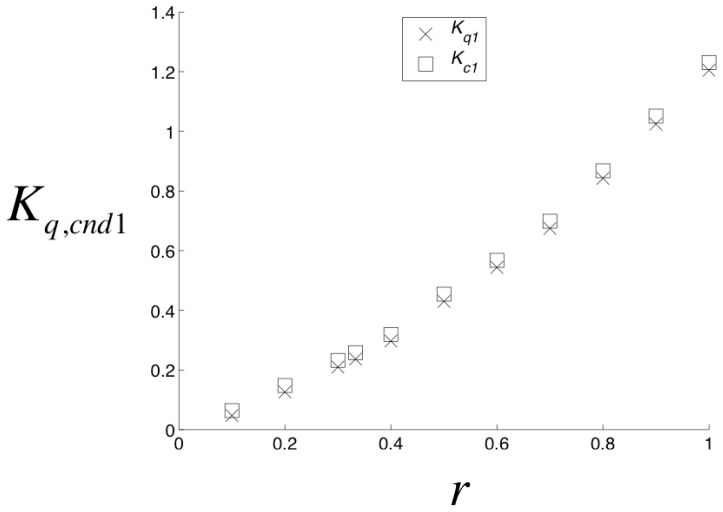

Figure 21. Comparison between PV and passive tracer diffusivities for simulations varying r in the upper layer.

The most appropriate values of C in this set of experiments are also limited to the interval [3.5, 4]. This is illustrated in Figures 22 and 23, which present a PV flux comparison showing the best coefficient C fit for simulations varying r in the upper layer.

For this evaluation, large domain simulations are not performed since there is close agreement between large and small domain simulations for the simulations varying β_{nd}.

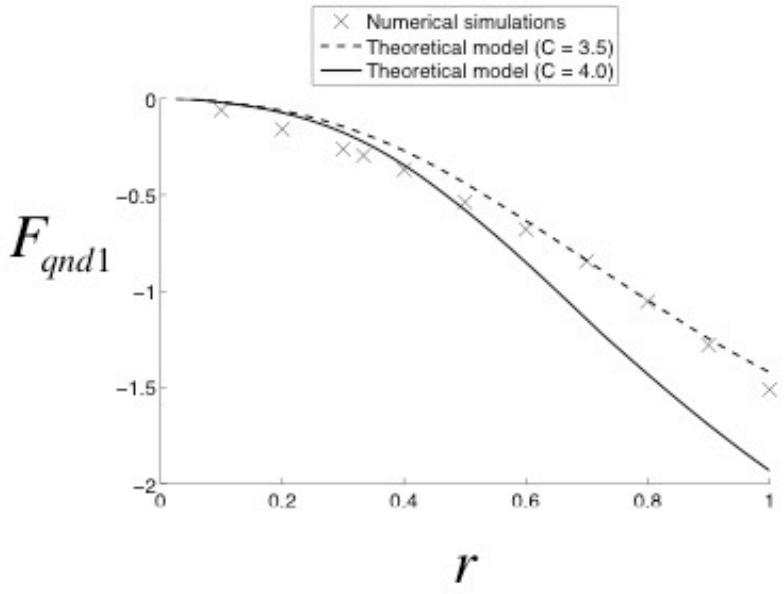

Figure 22. PV flux comparison showing the best coefficient *C* fit for simulations varying *r* in the upper layer.

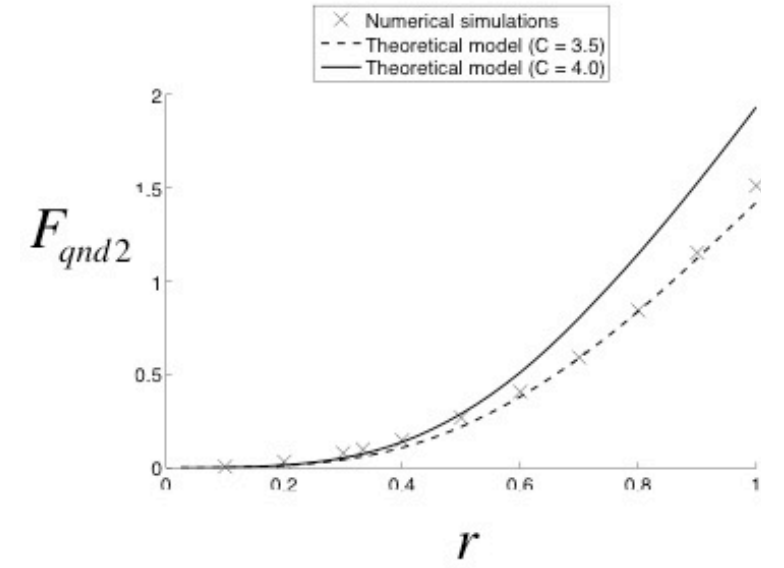

Figure 23. PV flux comparison showing the best coefficient *C* fit for simulations varying *r* in the lower layer.

D. SUMMARY

The objective of this chapter is to use a two-layer model configuration to validate and calibrate the GRB model. The Phillips problem is solved numerically and the equilibrated PV fluxes are, in turn, compared to the transport predicted by the GRB model. These numerical simulations explore the roles of two parameters (β_{nd} and r) in the equilibration of baroclinic instability. Equilibrated fluxes increase monotonically with faster flows, and preferably with WB flows. In addition, layers with comparable thicknesses have higher diffusivity. The differences between active and passive tracer fluxes are relevant only for very stable flows. Preliminary experiments with various values of bottom drag reveal that large-scale features can emerge in low-gamma regimes, and this effect is examined in greater detail in Chapter III. Finally, the values for the coefficient C (between 3.5 and 4) bound the solutions of the numerical model, and might be considered as appropriate inputs for the GRB model algorithm.

III. SCALE INTERACTIONS

The experiments described in Chapter II reveal that eddy-induced fluxes in simulations with low bottom drag fail to equilibrate as prescribed by the GRB model. The presence of eddies with length scales larger than the typical mesoscale eddies increase the equilibrated flux values and the variability around the equilibrium level. Recall that such large-scale features are referred to as Large-Scale Eddy Driven Patterns (LEDPs). The dependence of eddy-induced fluxes on the bottom drag coefficient is described in this chapter, which focuses on the identification of regimes in which the GRB model fails.

A. SCALE DECOMPOSITION

To distinguish between LEDPS and mesoscale eddies, we introduce the scale separator L_{ss} = 20 Rd representing wavelengths of 500 km. Here, Rd is the baroclinic radius of deformation for the two-layer model

$$Rd = \frac{1}{f}\sqrt{\frac{g'H_1H_2}{H_1+H_2}} \tag{33}$$

which controls the size of eddies formed directly as a result of baroclinic instability. Eddies with scales less (greater) than L_{ss} are classified as mesoscale (LEDPs). The corresponding critical horizontal wavenumber of separation κ_{cr} is evaluated as follows. Recall that

$$Rd_1 = \frac{1}{f}\sqrt{g'H_1} \tag{34}$$

what implies that

$$Rd = \frac{Rd_1}{\sqrt{1+r}} \tag{35}$$

and therefore

$$Rd_{nd} = \frac{Rd}{Rd_1} = \frac{1}{\sqrt{1+r}} \tag{36}$$

corresponds to the value of Rd when the lower layer thickness is much greater than the one for the upper layer. The expression of κ_{cr} in non-dimensional units is given by

$$\kappa_{cr\_nd} = \frac{2\pi}{wavelength_{nd}} = \frac{2\pi}{20Rd_{nd}} = \frac{2\pi R_{d1}}{20R_d} = 0.1\pi\sqrt{1+r} \tag{37}$$

where the scale separation

$$SS = \frac{\kappa_{cr\_nd}}{2\pi} = \frac{\sqrt{1+r}}{20} \tag{38}$$

is used in the Fourier analysis.

The GRB model attempts to predict the value at which eddy-induced fluxes equilibrate by focusing on the dynamics of mesoscale variability. However, depending on the choice of background parameters, the eddy field may be affected or even dominated by large-scale variability, bringing into question the relevance of the GRB model. Three different simulations illustrate this behavior in the upper layer PV perturbation field. In Figure 24a, the simulation with the largest non-dimensional bottom drag coefficient (γ_{nd} = 0.5) is shown. Nearly 30 eddies are aligned along the zonal direction that extends 3,750 km. Thus, these eddies have length scales of hundreds of kilometers, and only typical mesoscale features are present. In Figure 24b, a simulation with stronger (by a factor of two) background flow—implemented by halving the non-dimensional vorticity gradient—is shown. Mesoscale eddies still exist, but it can be seen that features of larger length scales are present. They show up as a group of blue colors in the left side of the basin, and a group of red colors at the right side. In Figure 24c, a simulation where the bottom drag coefficient has been decreased by two orders of magnitude is shown. A large-scale feature dominates the basin and suppresses all noticeable mesoscale variability.

The flow decomposition into mesoscale and LEDPs performed with the chosen scale separation L_{ss} is also shown in Figure 24. In the first simulation (Figure 24a), the mesoscale field is almost identical to the total field with large-scale transport responsible for approximately 1% of the total, and the GRB model fully predicts equilibrated fluxes. In the second simulation (Figure 24b), mesoscale features clearly still exist in the mesoscale plot, but the large-scale features become relevant. Their presence increases the LEDP transport to nearly 16% of the total PV transport. The GRB model can describe the development of instabilities from rest to equilibration, but the actual value of equilibrated

fluxes is missed. In the third simulation (Figure 24c), the LEDP field is the one that best resembles the total field. LEDPs are all over the basin, and they are responsible for approximately 99% of all eddy-induced transport. The GRB fails to describe eddy development both quantitatively and qualitatively. This last result is dramatic, and extra simulations can help to assess which regimes are more susceptible to LEDP dominance.

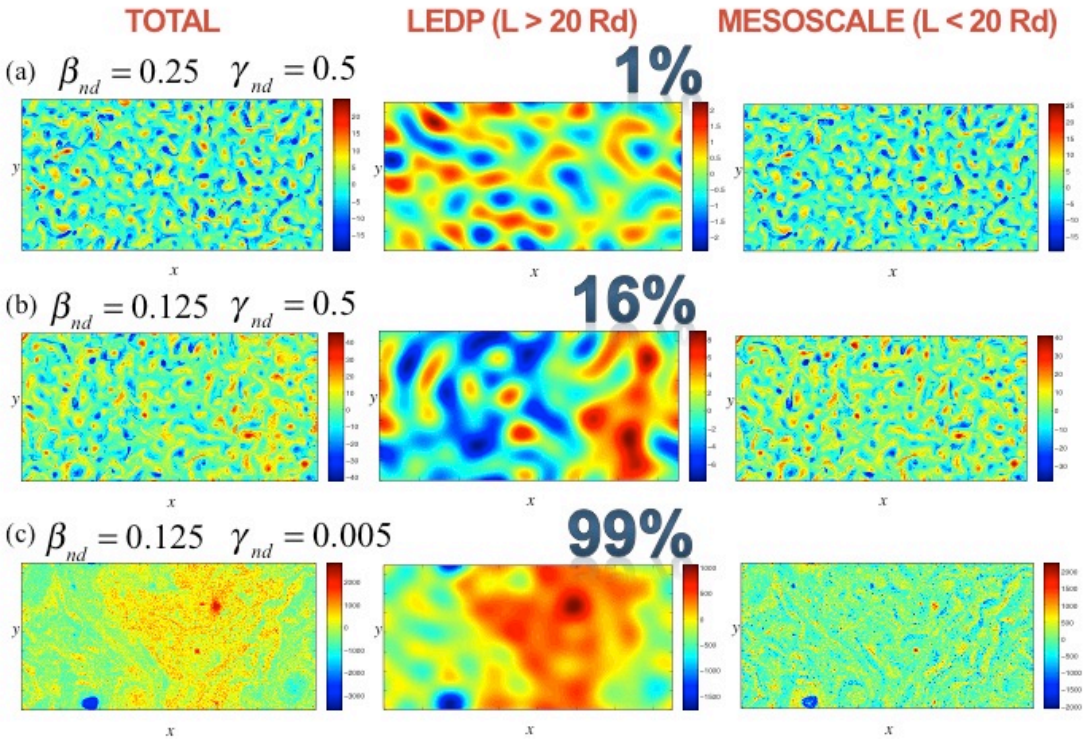

Figure 24. Upper layer PV perturbations from three different simulations divided into total, LEDP, and mesoscale fields. Percentages correspond to the portion of the eddy-induced transport carried by LEDP.

B. LEDP REGIMES

A framework needs to be developed to identify which regimes of equilibrated fluxes can be predicted using the GRB model. This is accomplished by introducing the discriminator variable

$$R = \ln\left(\frac{F_{q1LEDP}}{F_{q1MESO}}\right) \tag{39}$$

which compares the transports induced by LEDP and by mesoscale features. The natural logarithm is used to indicate LEDP dominance when R is positive, and mesoscale dominance when R is negative.

The dependence of mesoscale variability on LEDP regimes is examined through 40 numerical simulations, each with a different γ_{nd} taken from the range [0.5, 0.005], and different strength of background flow (quantified through $s\beta_{nd}$ taken from the range [-0.5, 0.25]). Figure 25 presents an interpolation of the discriminator variable R. It clearly shows that increasing bottom drag reduces the production of LEDPs. In the horizontal axis, faster flows occur toward β_{nd} = 0 (note that the zero is slightly displaced to the right). Results show that the stronger the flow, the more LEDP production is induced. WB flows (negative values of $s\beta_{nd}$) have a greater tendency to develop LEDP. Such flows are naturally counteracted by the rotation of the Earth, so they would need less energy to enter into a turbulent regime. The white line marks the values for R close to zero with any regime inside this dome having positive R. The GRB model fails to describe mesoscale eddy-induced flux equilibration in these regimes since it misses a large part of the turbulent transport performed by LEDPs.

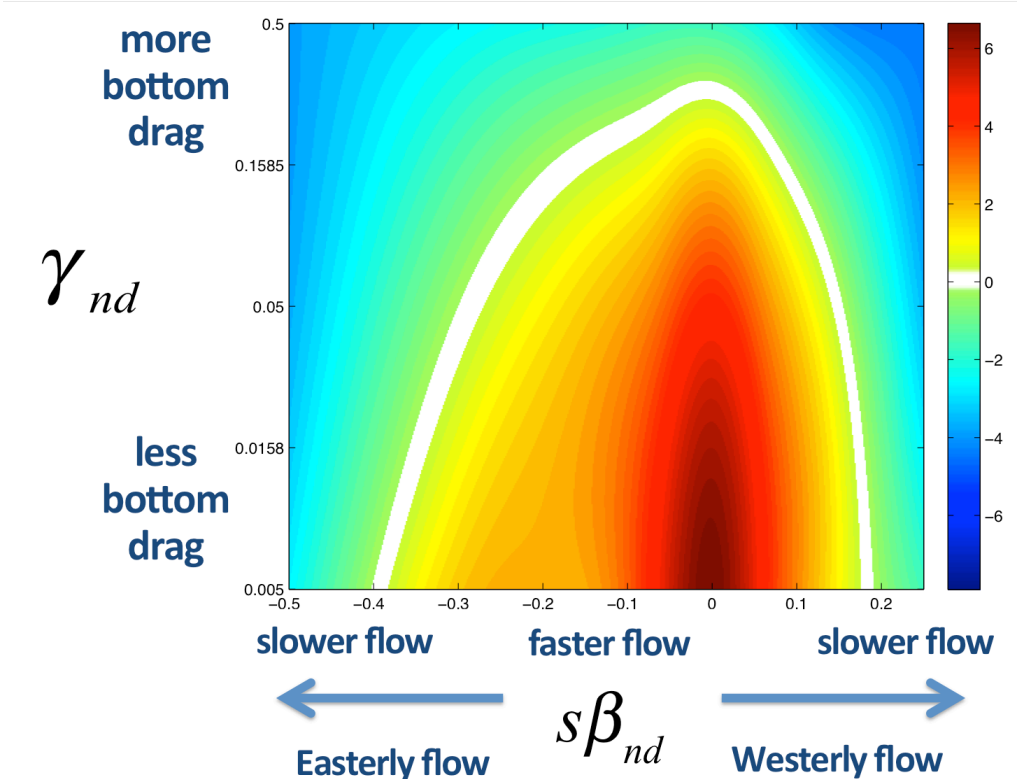

Figure 25. Discriminator *R* between LEDP and mesoscale eddy-induced PV fluxes. Reddish colors inside the white dome represent LEDP-dominant regimes.

C. SUMMARY

This objective of this chapter is to identify those regimes where the GRB fails to predict mesoscale eddy development (due to the presence of LEDPs). The Fourier analysis of 40 different simulations is conducted to divide the total fields of PV perturbations into mesoscale and LEDP fields. A scale separation is based on 20 radius of deformation. A discriminator *R* is introduced to identify regimes in which LEDP fluxes are larger than mesoscale fluxes. Finally, it is shown that strong, westward background flows and low bottom drag coefficients favor LEDP development.

THIS PAGE INTENTIONALLY LEFT BLANK

IV. HEAT TRANSPORT IN A CONTINUOUSLY STRATIFIED MODEL

The two-layer model validated the GRB theory, but it remains to be determined whether it is sufficiently general or configuration dependent. Therefore, we now turn to a different and more realistic setup—the continuously stratified problem formulated by Eady (1949). Numerical solutions are obtained using a three-dimensional model (MITgcm) and compared with the predictions of GRB theory. This comparison demonstrates that its key assumptions (a balance between growth rates of primary and secondary instabilities) is generic and is likely to apply to different models.

The diagnostics are focused on RMS velocity and heat flux since they are computed from a second order statistical moment that represents variability around the mean. The analysis of the PV fluxes (an approach used for the Phillips configuration in Chapter II) becomes less meaningful for the Eady configuration, which is characterized by zero meridional background PV gradients. The RMS velocity profiles also indicate the amount of eddy kinetic energy available at each vertical layer. The analysis of the numerical model and validation of the GRB model in this chapter follows three steps. First, equilibration is simulated in the three-dimensional model to qualitatively verify the dynamics assumed by the GRB model. Second, the Eady problem is solved using the GRB algorithm, and the solutions are expressed in terms of RMS horizontal velocity profiles. Finally, the RMS horizontal velocities computed at each vertical layer in the three-dimensional numerical model are compared with the RMS horizontal velocity profiles from the GRB theory. The agreement suggests that the GRB model is able to predict eddy equilibration in this more realistic environment.

A. NUMERICAL MODEL DESCRIPTION

Eddy development is induced in the three-dimensional model by baroclinic instability, which is introduced as follows. The temperature is relaxed to the prescribed temperature profiles at the warm Southern boundary and the cold Northern boundary of the domain. The resulting meridional density gradients cause vertical shear of the zonal

flow through thermal wind effect, which, in turn, generates baroclinic instability. The target temperature at the boundaries decreases linearly with depth and the overall vertical variation in temperature is $\Delta_z \overline{T}$ = -5˚C. The model domain is a cuboid with dimensions extending 1024 km horizontally (a square) and 1100 m vertically. The eddy-resolving horizontal grid spacing is 2 km. The domain spans through 44 vertical levels spaced 25 m apart from 0 to 1075 m and periodic boundary conditions are applied in the zonal direction. The interior temperature is allowed to fluctuate under the influence of mesoscale eddies.

The meridional temperature gradient produces mean horizontal velocity and typical mesoscale flows. The basic configuration assumes the background flow U = 0.1 ms^{-1} at the surface and the radius of deformation Rd approximately 33 km. The background flow is computed from

$$\overline{U} \sim \frac{\partial U}{\partial z}(H+z) \tag{40}$$

for each layer of depth z. The basin depth is H = 1100 m. The vertical shear caused by thermal wind is

$$\frac{\partial \overline{U}}{\partial z} = \frac{g}{f}\frac{1}{\rho}\frac{\partial \rho}{\partial y} \tag{41}$$

where g = 9.81 ms^{-2}, and f = 10^{-4} s^{-1}. The simplified equation of state takes the form

$$\frac{\Delta\rho}{\rho} = -\alpha.\Delta T \tag{42}$$

where the thermal expansion coefficient α = 2 x 10^{-4} ˚C^{-1} and target meridional variation in temperature $\Delta_y \overline{T}$ = -5˚C (warmer South, colder North, negative gradient). The salinity contraction coefficient is set to zero so that all effects on the density distribution are controlled entirely by the temperature component. The buoyancy frequency is given by

$$N_b = \sqrt{\frac{g}{\rho}\frac{\partial \rho}{\partial z}} \tag{43}$$

and the radius of deformation is

$$R_d = \frac{N_b H}{f}. \tag{44}$$

The eddy-induced heat flux is computed according to

$$F_T = \langle T'V' \rangle \tag{45}$$

and its time record makes it possible to observe the instability growth from rest to equilibration. In (45), F_T depends on the anomalies of temperature T' and meridional flow V' while the angular brackets represent the spatial mean at each vertical level. The temperature relaxation zones are excluded by considering only the inner 80% of the domain in the meridional direction.

Figures 26 and 27 present a typical simulation of baroclinic instability in the continuously stratified model. The dynamics of equilibration are clearly illustrated by the numerical model. Figure 26 shows the time record of the heat transport by eddies at the surface. Initially, the heat flux is zero, and it continuously increases in time as unstable temperature and velocity perturbations grow. Figure 27 presents four successive snapshots of temperature perturbation. The temperature field is initially at rest (Figure 27a, t = 0). The background flow develops nearly as expected from thermal wind balance after several days, and instabilities organize in baroclinic wave modes between three (Figure 27b) and four months (Figure 27c). Equilibrium is achieved after six months. (Figure 27d).

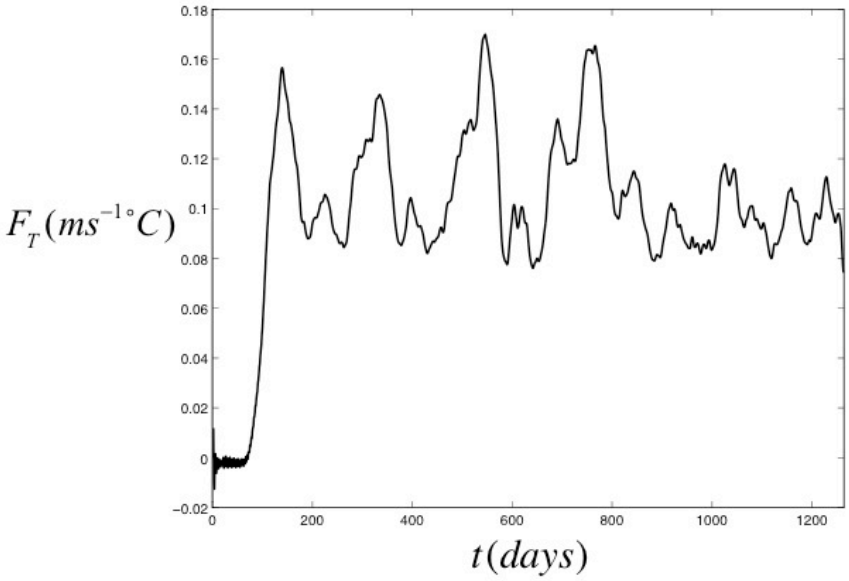

Figure 26. Eddy-induced heat flux time record in days.

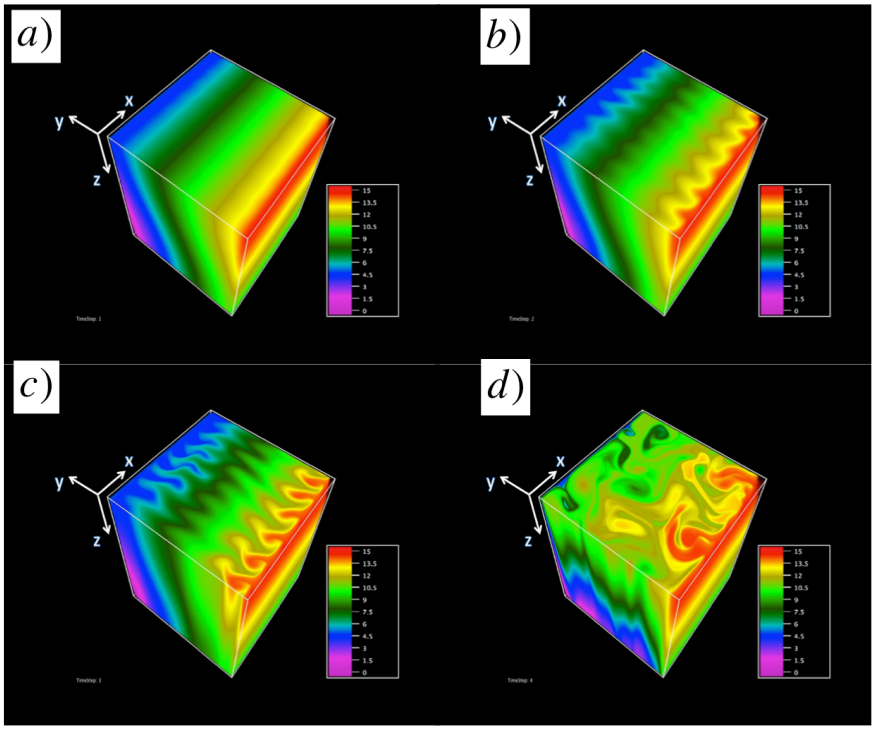

Figure 27. Snapshots of the temperature anomaly field development.

B. GROWTH RATE BALANCE THEORY

1. Formulation of the Eady Model

The Eady model solves the governing equation

$$\frac{\partial}{\partial t}\nabla^2\psi + J(\psi,\nabla^2\psi) + z\frac{\partial}{\partial x}\nabla^2\psi = 0 \tag{46}$$

subject to the bottom z = -1 and the surface z = 0 boundary conditions

$$\frac{\partial^2\psi}{\partial t\,\partial z} + J(\psi,\frac{\partial\psi}{\partial z}) + z\frac{\partial^2\psi}{\partial x\,\partial t} - \frac{\partial\psi}{\partial x} = 0, z = -1,0 \tag{47}$$

for the perturbation streamfunction (ψ). The streamfunction Ψ and the corresponding zonal velocity $\bar{U}$ describe the basic state as in

$$\bar{U} = -\frac{\partial\Psi}{\partial y} \tag{48}$$

$$\Psi = -\bar{U}y = -\frac{U(H+z)}{H}y\,. \tag{49}$$

The system is converted to non-dimensional units by using the radius of deformation, the background flow at the surface, and the basin depth. The key result of the Eady (1949)

analysis is the calculation of the linear growth rates of primary baroclinic instabilities as a function of background parameters.

2. Implementation of the GRB Theory

The aforementioned experiments with the three-dimensional model show that the key assumptions of the GRB theory are realized in a continuously stratified model. However, for further verification, it is necessary to compare the amplitude of the baroclinic waves in the numerical model with that in the theory. The details of the GRB implementation for the Eady problem are not presented since they are analogous to that for the Phillips model (Chapter II). The output is given in terms of the equilibrium RMS velocity profiles. The specific values depend upon the assumed coefficient C.

3. Sensitivity of Solutions to the GRB Coefficient *C*

The RMS velocity profiles are computed from the solutions of the Eady problem for the perturbation streamfunction. Figure 28 shows typical RMS velocity profiles for different coefficient C values. The variability minimum is observed in the middle of the vertical extent of the basin (z = -0.5) while it increases towards similar maximum values at the surface and at the bottom. The magnitude of the RMS velocity increases monotonically with increasing C.

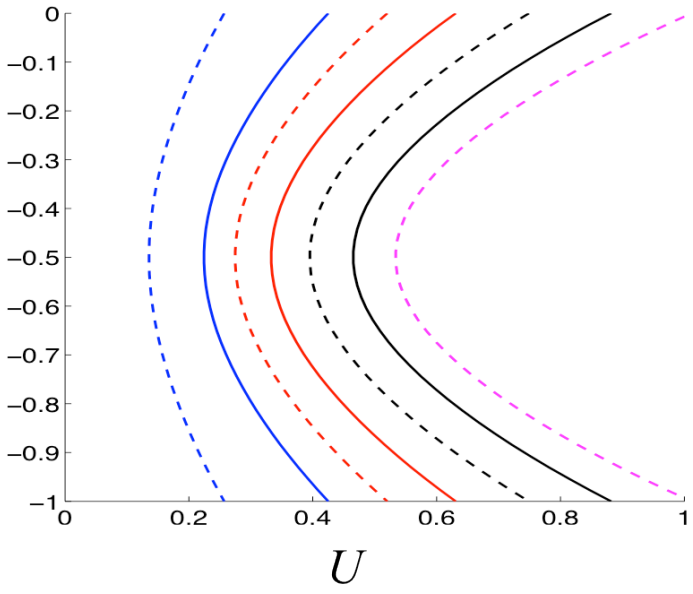

Figure 28. RMS velocity profiles for different coefficient *C* values. Both axes are non-dimensional.

C. COMPARISON OF THE THEORETICAL AND NUMERICAL MODELS

The comparison is based on four simulations with different background flows and stratifications. In the first simulation, the target variations in temperature are set $|\Delta_y \bar{T}|$ = 5˚C and $|\Delta_z \bar{T}|$ = 5˚C. In the second, the target meridional variation in temperature is doubled, which doubles the background flow. In the third, the target vertical variation in temperature is doubled, which increases the radius of deformation. In the final simulation both meridional and vertical gradients are doubled. For each experiment, the RMS velocity profiles are compared (Figure 29) to solutions for the equivalent Eady problem. Figure 29a presents the numerical simulations and the solutions of the Eady problem for $|\Delta_y \bar{T}|$ = 5˚C and $|\Delta_z \bar{T}|$ = 5˚C. The following figures present those for $|\Delta_y \bar{T}|$ = 5˚C and $|\Delta_z \bar{T}|$ = 10˚C (Figure 29b), $|\Delta_y \bar{T}|$ = 10˚C and $|\Delta_z \bar{T}|$ = 5˚C (Figure 29c), and $|\Delta_y \bar{T}|$ = 10˚C and $|\Delta_z \bar{T}|$ = 10˚C (Figure 29d).

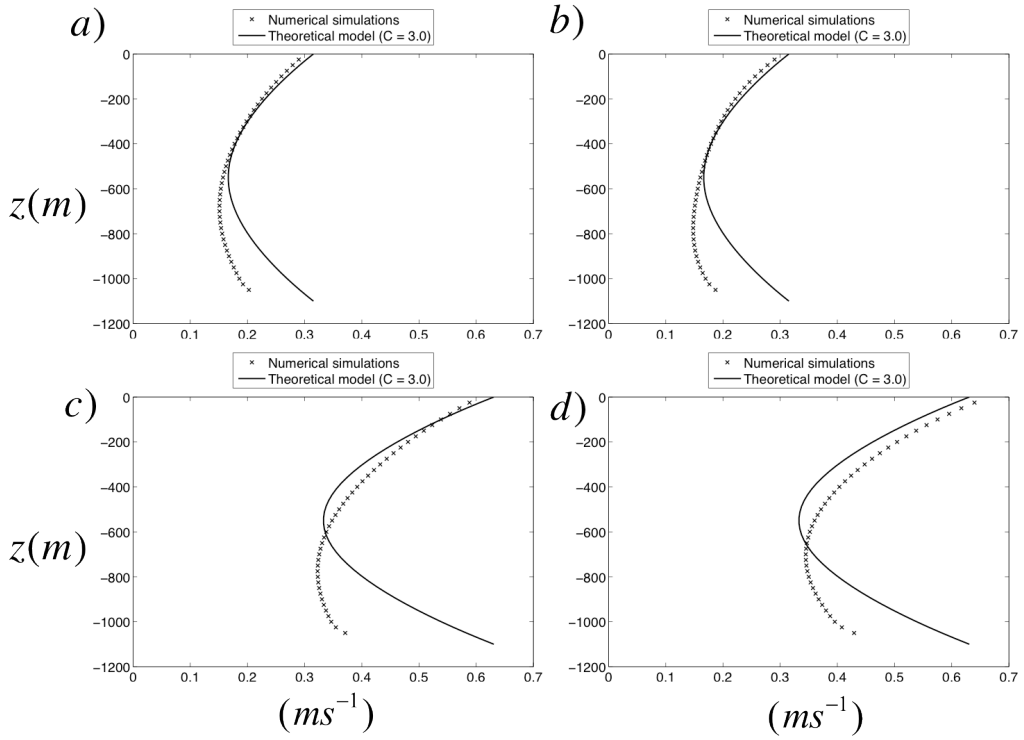

Figure 29. Comparison of RMS velocity profiles.

The RMS velocity profiles computed for the Eady model with coefficient $C = 3$ provide good fit to the RMS velocity profiles of the numerical model. This result matches the conclusion obtained earlier for the two-layer model configuration (Chapter II), in which the coefficient C lies between 3.5 and 4. The agreement is particularly good in the upper part of the water column. The reduced agreement toward the bottom of the profiles is related to the inclusion of bottom drag in the numerical model (necessary to prevent the spontaneous generation of large-scale features) whereas bottom drag is neglected in the Eady problem. It should also be noted that the Eady problem is formulated in an unbounded ocean. However, the results in Figure 29 indicate that the three-dimensional model can still provide appropriate comparison provided that the meridional extent is much larger than the radius of deformation.

D. SUMMARY

The objective of this chapter is to use a continuously stratified model to validate the GRB model in a scenario that is more realistic than the two-layer model. A three-dimensional numerical model (MITgcm) is employed to generate equilibrated heat fluxes. It is verified that the stages of eddy development are consistent with the assumptions of the GRB model. A comparison between the RMS velocity profiles in the numerical model and in the theory validates the GRB model as a convenient predictor of the intensity of mesoscale variability. Finally, the coefficient $C = 3$ obtained from the continuously stratified models is consistent with the corresponding estimates from the two-layer model.

V. ACOUSTIC SIGNATURES OF MESOSCALE VARIABILITY

The equilibration of eddy-induced fluxes predicted by the GRB theory in the continuously stratified model indicates the presence of a fully-developed mesoscale eddy field. This field represents a challenge for acoustic propagation prediction, and this is a very important naval problem. Comparing two different moments in the simulations helps to understand some characteristics of this problem. The first is when the ocean is still unperturbed, called an eddy-poor scenario. The other is when fluxes are already equilibrated, called the eddy-rich scenario.

A. ENVIRONMENTAL DATA

The temperature data from the three-dimensional model is applied to characterize the eddy field. A simulated ship collects 21 along-track temperature profiles starting from the South and going North in the zonal center of the basin as in Figure 30. The profiles are spaced 40 km apart and extend from the surface to the bottom. The track keeps 10% of the meridional extent away from each meridional boundary.

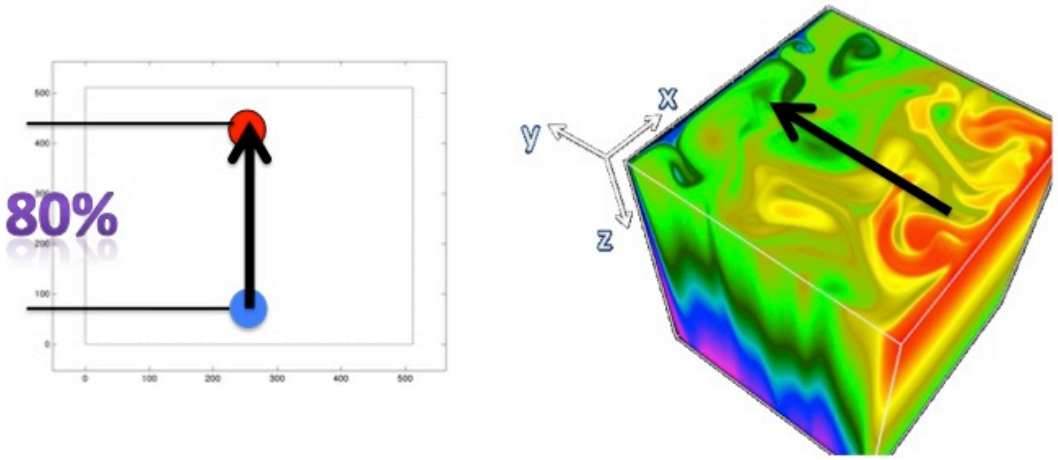

Figure 30. Simulated ship track.

This analysis intends to avoid any bottom interaction that could mislead the acoustic signature from eddy effects. However, the computational cost of extending the basin vertically beyond the 1100 m available in the MITgcm data would sacrifice the 25

m vertical resolution. The solution is to mount the temperature profiles over an isothermal layer extending from 2000 m to 4000 m. The bottom temperature of the MITgcm model is relaxed to the isothermal layer temperature linearly with depth between 1100 m and 2000 m. Although this procedure introduces new data to the MITgcm model results, all analysis is limited to the upper 1000 m eddy field.

Another point is the salinity contraction coefficient of the equation of state that is set to zero for the GRB validation. The salinity profiles are necessary to compute sound speed profiles, so climatology for the ACC region in January is obtained from the Naval Research Lab (NRL) Generalized Digital Environmental Model (GDEM). This provides a realistic and detailed profile for a known turbulent region. Once the temperature and salinity profiles are available, the sound speed profiles (SSP) are computed using a MATLAB code for the nine-term Mackenzie equation (Mackenzie 1981) and then processed with the Bellhop acoustic toolbox (Porter and Bucker 1987). Sample profiles are provided in Figure 31.

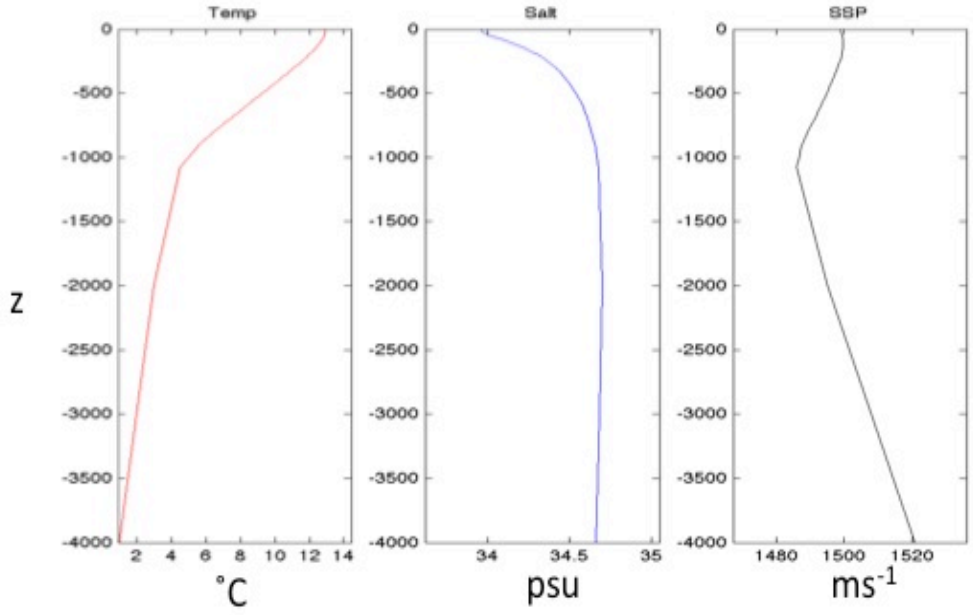

Figure 31. Sample profiles of temperature, salinity, and sound speed.

The temperature cross-sections and the range-dependent sound speed profiles for each scenario are shown in Figures 32 and 33. In the eddy-poor scenario, the South is warm, the North is cold, and the temperature decreases with depth. These temperatures affect the sound speed profiles by increasing sound speed in the South, and decreasing in the North. Overall, the fastest sound speed velocities are close to the bottom due to the effect of pressure. In the eddy-rich scenario, warm core and cold core eddies are very well defined. The same sound speed dependence on temperature is observed. A rough observation of the features in this 800-km cross section shows that there are eddies extending between 50 and 100 km each, so they clearly represent mesoscale eddies.

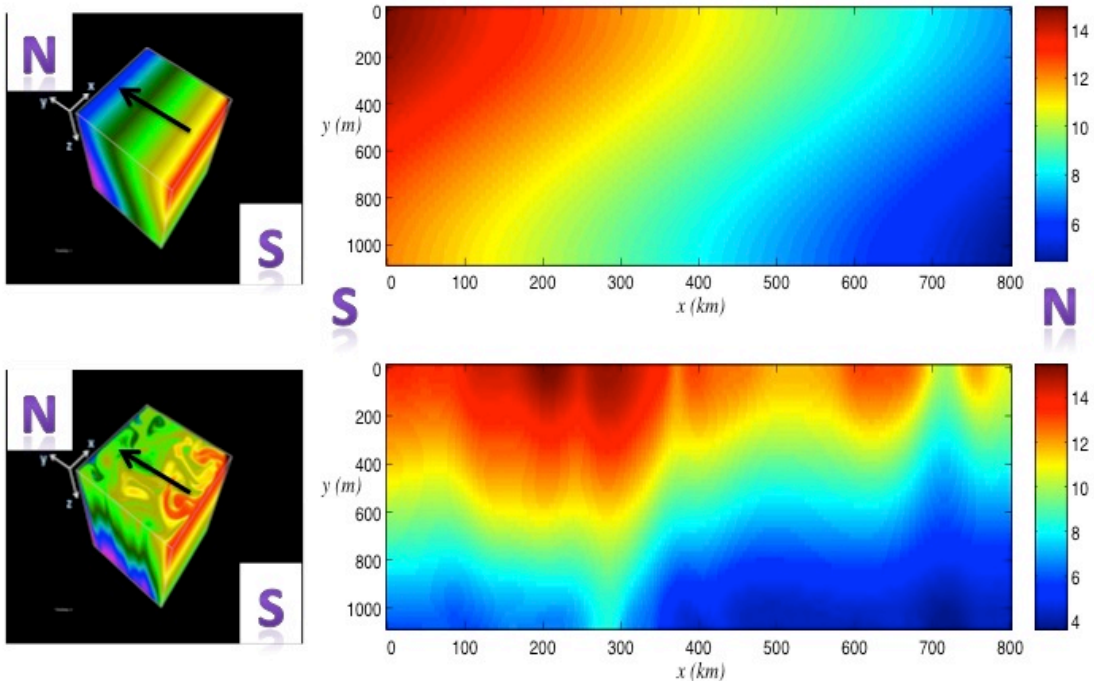

Figure 32. Along-track temperature cross sections for the eddy-poor (above) and the eddy-rich scenarios.

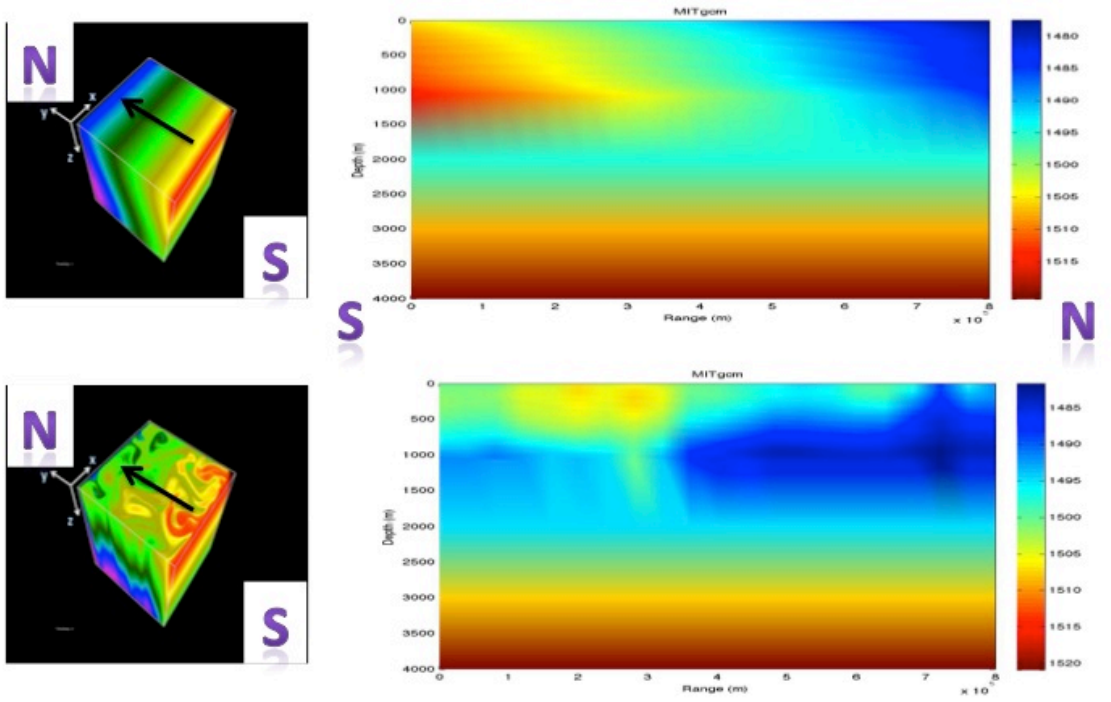

Figure 33. Along-track range-dependent sound speed surfaces for the eddy-poor (above) and the eddy-rich scenarios.

B. ACOUSTIC SIGNATURES

1. Configuration

After some simulations, it seems that launching seven acoustic rays yields less busy ray tracing plots. The launching angles are equally spaced between five degrees above and below the horizontal plane of the source. The analysis is performed for three different source depths at 5 m, 250 m, and 1000 m. It should be noted that the ray paths and transmission losses are also valid if the problem is inverted and a receiver is placed in the position of the source. The source frequency is 200 Hz. Figures 34 through 36 are Bellhop plots for the sound speed surfaces at the top, ray tracing in the center, and transmission losses at the bottom.

2. Acoustic Signatures for a Near-Surface Source

In the eddy-poor scenario, the ray tracing plots show that the acoustic propagation in an unperturbed ocean depends mostly on the launching angle. In the eddy-rich scenario, the warm core eddies act to bend down the acoustic rays and create an acoustic

shadow that can be tactically explored. The colder mid-depth temperatures act to bend the acoustic rays back to the surface. Finally, the far cold core eddies act to concentrate the acoustic energy, creating a possible extended-range detection, depending on the power of the source. The TL plots help to identify the acoustic shadow position.

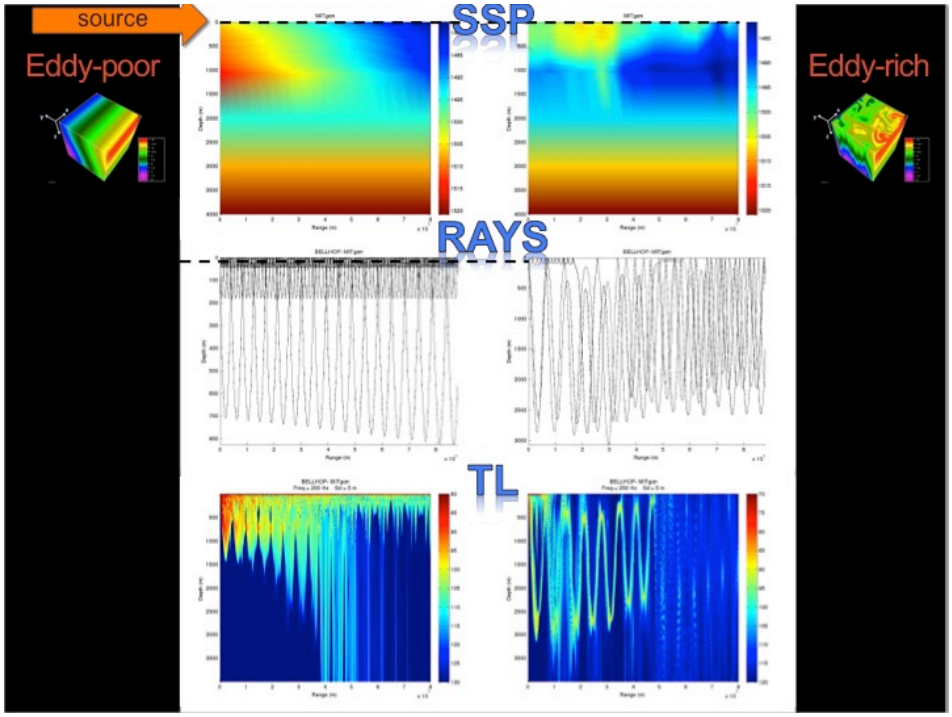

Figure 34. An acoustic signature of mesoscale eddies for a source depth of 5 m.

3. Acoustic Signatures for a Mid-depth Source

The eddy-poor scenario presents the same behavior for a near-surface source, but the eddy-rich scenario is quite different. The lower source depth at 250 m permits an acoustic emission exactly through the vertical center of the near-source warm core eddies. The acoustic rays are now able to propagate through the eddy, especially those with very small launching angles. Possibly, this is a well-suited depth to lower the source (or receiver) if it is necessary to detect a target present inside an acoustic shadow created by a warm core eddy.

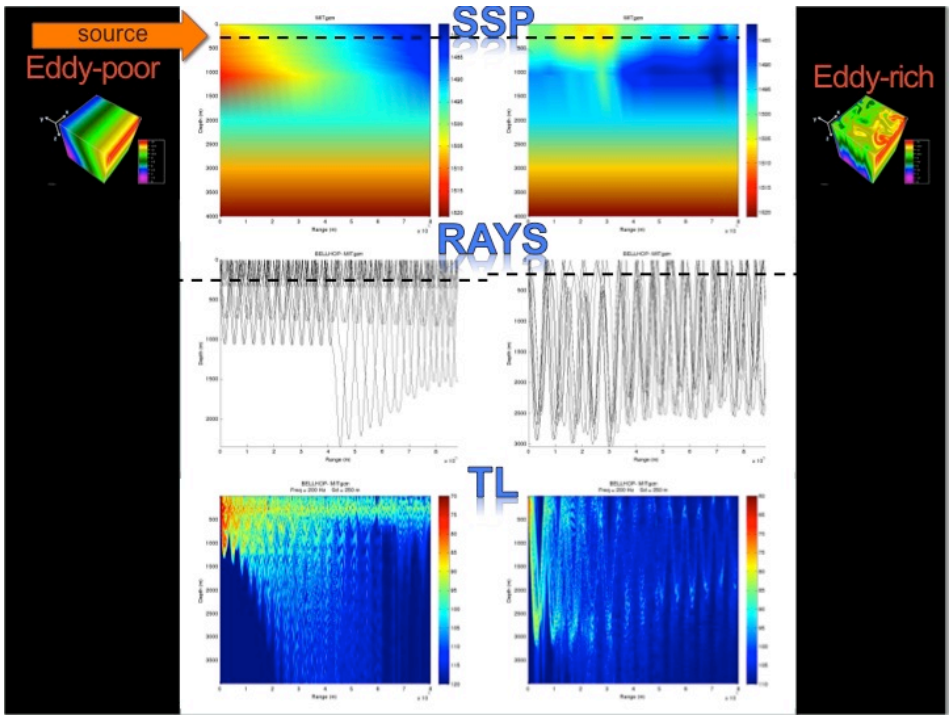

Figure 35. An acoustic signature of mesoscale eddies for a source depth of 250 m.

4. Acoustic Signatures for a Deep Source

Finally, the source depth is lowered to 1000 m, so the acoustic rays miss the surface eddies. The shallow warm core eddies are not able to greatly interfere in the propagation pattern. The natural bending up of the rays caused by the colder temperatures, associated with the far-located cold core eddies, extend the surface detection. The comparison between the transmission losses in the two scenarios resembles well this extended range.

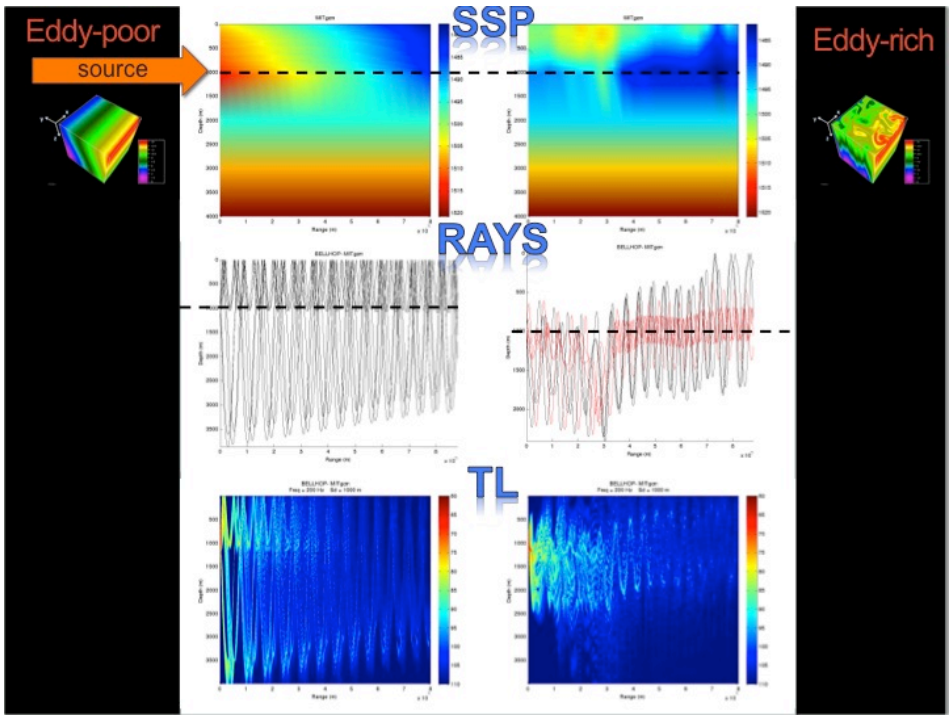

Figure 36. An acoustic signature of mesoscale eddies for a source depth of 1000 m.

C. SUMMARY

Accurate acoustic prediction in range-dependent environments is a very complex problem that is sensitive to proper characterization of the eddy field scale and gradients. This is a very brief analysis of the acoustic signatures of the equilibrated mesoscale eddy field predicted by the GRB model, but the objective is achieved. Mesoscale eddies greatly affect the acoustic propagation, so they deserve appropriate characterization.

THIS PAGE INTENTIONALLY LEFT BLANK

VI. CONCLUSIONS

The GRB model is a new equilibration theory capable of predicting equilibrated eddy-induced fluxes. It describes development of eddies as a result of baroclinic instability from initial perturbations to a fully developed eddy-field. The model attributes the equilibration of instability to a competition between primary and secondary instabilities. The equilibration is achieved when the growth rate of primary instabilities is comparable to the growth rate of secondary instabilities. The basis for such an assumption is the observation that baroclinic instability modes emerging from random perturbations grow in time and develop secondary instabilities. Unlike the primary ones, the growth rate of secondary instabilities monotonically increases with the amplitude of primary modes. At first, the growth of secondary instabilities is too slow to inflict any significant damage to growing primary modes—the evolution of small-amplitude perturbations is adequately captured by the linear theory. However, at some point, the growth rate of secondary instabilities significantly exceeds the primary growth rates. As a result, the secondary instabilities gain in magnitude, rapidly reaching the level of primary modes, and suppress their growth. At this stage, the system reaches statistical equilibrium. This GRB assumption leads to analytical solutions of eddy development that can ultimately replace the classic parameterization of equilibrated eddy-induced fluxes.

Based on the GRB model, a simple algorithm is developed which predicts the equilibrium eddy-induced fluxes and RMS velocity as functions of background parameters. First, the growth rate of primary instabilities is computed using the linear instability theory (Eady 1949; Phillips 1951). Second, the Floquet theory for the stability of boundary layer flows (Herron 1984) is used to compute the growth rate of secondary instabilities based on the amplitude of the primary instabilities. Finally, the growth rate balance (1) determines the equilibrium amplitude of mesoscale variability. The GRB model is verified by comparing several predictions like meridional PV fluxes, eddy diffusivities and RMS velocity profiles with the corresponding numerical results. Such

comparisons are made for a two-layer model (Chapter II), and a continuously stratified model (Chapter IV). The coefficient *C*, with values between 3 and 4, guarantees the growth rate balance between primary and secondary instability growth rates.

The two-layer system is used to explore the dependences of equilibrated fluxes on three characteristics of the background flow: β_{nd}, r and γ_{nd}. The eddy-induced transport is largest for small negative values of non-dimensional vorticity gradient and large thickness ratio. A series of simulation with varying γ_{nd} show that the development of large-scale features in some regimes can cause failure of the GRB model. Such regimes are realized for small negative values of non-dimensional vorticity gradient and low bottom drag coefficient. It must be pointed out that the GRB model is very general. In this study it has been applied to baroclinic instability, but it is possible that it can address other theoretical instability problems in fluid dynamics.

Finally, an acoustic analysis (Chapter V) attempts to quantify the influence of mesoscale eddies on sound propagation in the ocean. The comparison between acoustic signatures of eddy-poor and eddy-rich scenarios suggests that fully-developed eddy fields greatly affect acoustic propagation. Acoustic shadows and range-extended propagation exemplify the influences of the presence of eddies in the ocean environment.

VII. RECOMMENDATIONS

The results of this work motivate a number of different studies to follow. Hence, the list below comprises suggestions for future research topics:

1. The validation of the GRB model in non-zonally oriented basins
2. More detailed analysis of the dynamics and transport characteristics of variability in the LEDP-dominated regimes
3. Effects of variable bottom topography on eddy dynamics and equilibrium transport
4. In depth acoustic analysis of equilibrated mesoscale eddy fields

THIS PAGE INTENTIONALLY LEFT BLANK

LIST OF REFERENCES

Balmforth, N. J., and Y.-N. Young, 2002: Stratified Kolmogorov flow. *J. Fluid Mech*., **450**, 131–167.

Balmforth, N. J., and Y.-N. Young, 2005: Stratified Kolmogorov flow. Part 2. *J. Fluid Mech*., **528**, 23–42.

Charney, J. G., 1947: The dynamics of long waves in a baroclinic westerly current. *J. Meteor.,* **4**, 135–162.

Eady, E. T., 1949: Long waves and cyclone waves. *Tellus*, **1**, 33–52.

Eden, C., 2011: A closure for meso-scale eddy fluxes based on linear instability theory. *Ocean Modelling*, **39**, 362–369.

Frisius, T., 1998: A mechanism for the barotropic equilibration of baroclinic waves. *J. Atmos. Sci.*, **55**, 2918–2936.

Gent, P. R., and J. C. McWillliams, 1990: Isopycnal mixing in ocean circulation models. *J. Phys. Oceanogr.*, **20**, 150–155.

Gill, A. E., 1982: *Atmosphere-Ocean Dynamics*. Academic Press, 662 pp.

Held, I. M., and V. D. Larichev, 1996: A scaling theory for horizontally homogeneous, baroclinically unstable flow on a beta plane. *J. Atmos. Sci.*, **53**, 946–952.

Henning, C. C., and G. K. Vallis, 2005: The effects of mesoscale eddies on the stratification and transport of an ocean with a circumpolar channel. *J. Phys. Oceanogr.*, **35**, 880–896.

Herron, I. H., 1984: Floquet theory for the stability of boundary layer flows. *J. Approximation Theory*, **42**, 387–406.

Kamenkovich, I., P. Berloff, and J. Pedlosky, 2009: Role of eddy forcing in the dynamics of multiple zonal jets in a model of the North Atlantic. *J. Phys. Oceanogr.*, **39**, 1361–1379.

Kimura, S. and W. Smith, 2011: Secondary instability of salt sheets. *J. Mar. Res.*, **69**, 57–77.

Lapayere, G. and I. M. Held, 2003: Diffusivity, kinetic energy dissipation, and closure theories for the poleward eddy heat flux. *J. Atmos. Sci.*, **60**, 2907–2916.

Larichev, V. D., and I. M. Held, 1995: Eddy amplitudes and fluxes in a homogeneous model of fully developed baroclinic instability. *J. Phys. Oceanogr.*, **25**, 2285–2297.

Lévy, M., P. Klein, A. M. Tréguier, D. Iovino, G. Madec, S. Masson, and K. Takahashi, 2010: Modifications of gyre circulation by sub-mesoscale physics. *Ocean Modelling*, **34**, 1–15.

Lick, W., 1965: The instability of a fluid layer with time-dependent heating. *J. Fluid Mech*., **21**, 565–576.

Mackenzie, K.V., 1981: Nine-term equation for sound speed in the oceans. *J. Acoust. Soc. Am.*, **70**, 807–812.

Manfroi, A. J., and W. R. Young, 1999: Slow evolution of zonal jets on the beta plane. *J. Atmos. Sci.*, **56**, 784–800.

Manfroi, A. J., and W. R. Young, 2002: Stability of beta-plane Kolmogorov flow. *Phys. D*, **162**, 208–232.

Marshall, J., C. Hill, L. Perelman, and A. Adcroft, 1997a: Hydrostatic, quasi-hydrostatic, and nonhydrostatic ocean modeling. *J. Geophys. Res.*, **102**, 5733–5752.

Marshall, J., A. Adcroft, C. Hill, L. Perelman, and C. Heisey, 1997b: A finite-volume, incompressible Navier Stokes model for studies of the ocean on parallel computers. *J. Geophys. Res.*, **102**, 5753–5766.

Novikov, A., and G. Papanicolaou, 2001: Eddy viscosity of cellular flows. *J. Fluid Mech.*, **446**, 173–198.

Pedlosky, J., 1970: Finite-amplitude baroclinic waves. *J. Atmos. Sci.*, **27**, 15–30.

Pedlosky, J., 1971: Finite-amplitude baroclinic waves with small dissipation. *J. Atmos. Sci.*, **28**, 587–597.

Pedlosky, J., 1981: Nonlinear dynamics of baroclinic wave ensembles. *J. Fluid Mech.*, **102**, 169–209.

Pedlosky, J., 1987: *Geophysical Fluid Dynamics*. Springer-Verlag, 732 pp.

Phillips, N. A., 1951: A simple three-dimensional model for the study of large-scale extratropical flow patterns. *J. Meteor.*, **8**, 381–394.

Porter, M. B., and H. P. Bucker, 1987: Gaussian beam tracing for computing ocean acoustic fields. *J. Acoust. Soc. Am.*, **82**, 1349–1359.

Radko, T., 2011: On the generation of large-scale structures in a homogeneous eddy field. *J. Fluid Mech.*, **668**, 76–99.

Radko, T., 2012: Eddy viscosity and diffusivity in the modon-sea model. *J. Mar. Res.*, **69**, 723–752.

Radko, T., and I. Kamenkovich, 2011: Semi-adiabatic model of the deep stratification and meridional overturning. *J. Phys. Oceanogr.*, **41**, 757–780.

Radko, T., and J. Marshall, 2004: Eddy-induced diapycnal fluxes and their role in the maintenance of the thermocline. *J. Phys. Oceanogr.*, **34**, 372–383.

Radko, T. and D. P. Smith, 2012: Equilibrium transport in double-diffusive convection, *J. Fluid Mech.*, **692**, 5–27.

Radko, T., and M. E. Stern, 1999: Salt fingers in three dimensions. *J. Mar. Res.*, **57**, 471–502.

Rhines, P. B., and W. R. Young, 1982: A theory of the wind-driven circulation. I. Mid-ocean gyres. *J. Mar. Res.*, **40**, 559–596.

Robinson, A. R., 1983: *Eddies in Marine Science*. Springer-Verlag, 609 pp.

Robinson, J. L., 1976: Theoretical analysis of convective instability of a growing horizontal thermal boundary layer. *Phys. Fluids*, **19**, 778–791.

Sivashinsky, G., 1985: Weak turbulence in periodic flows. *Phys. D*, **17**, 243–255.

Spall, M. A. and D. C. Chapman, 1998: On the efficiency of baroclinic eddy heat transport across narrow fronts. *J. Phys. Oceanogr.,* **28**, 2275–2287.

Talley, L., G. Pickard, W. Emery, and J. Swift, 2011: *Descriptive Physical Oceanography: An Introduction*. Academic Press, 555 pp.

Thompson, A. F., and W. R. Young, 2006: Scaling baroclinic eddy fluxes: Vortices and energy balance. *J. Phys. Oceanogr.,* **36**, 720–738.

Thompson, A. F., and W. R. Young, 2007: Two-layer baroclinic eddy heat fluxes: Zonal flows and energy balance. *J. Atmos. Sci.*, **64**, 3214–3231.

Visbeck, M., J. Marshall, and T. Haine, 1997: Specification of eddy transfer coefficients in coarse-resolution ocean circulation models. *J. Phys. Oceanogr.,* **27**, 381–402.

Wolfe, C. L., and P. Cessi, 2010: What sets the strength of middepth stratification and overturning circulation in eddying ocean models? *J. Phys. Oceanogr*., **40**, 1520–1538.

Wolfe, C. L., and P. Cessi, 2011: The adiabatic pole-to-pole overturning circulation. *J. Phys. Oceanogr.,* **41**, 1795-1810.

INITIAL DISTRIBUTION LIST

1. Defense Technical Information Center
   Ft. Belvoir, Virginia

2. Dudley Knox Library
   Naval Postgraduate School
   Monterey, California